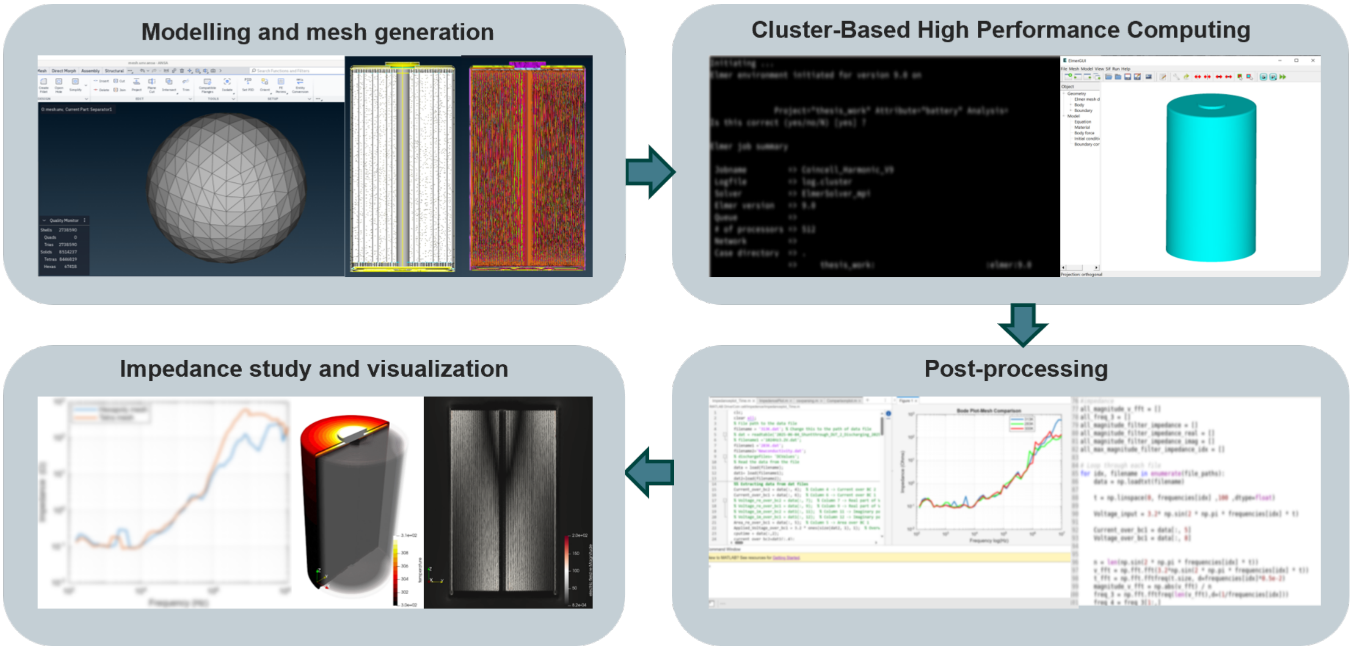

Realistic Modelling of Li-ion Batteries for Calculating High Frequency Impedance

EENX30 - Master of Science Thesis

ADITHYA SIVAKUMAR
SURESH CHANDER DURAIVEL

Department of Electrical Engineering
Division of Electric Power Engineering
CHALMERS UNIVERSITY OF TECHNOLOGY
Gothenburg, Sweden 2025
www.chalmers.se

MASTER'S THESIS 2025

Realistic Modelling of Li-ion Batteries for Calculating High Frequency Impedance

ADITHYA SIVAKUMAR
SURESH CHANDER DURAIVEL

Department of Electrical Engineering
Division of Electric Power Engineering
CHALMERS UNIVERSITY OF TECHNOLOGY
Gothenburg, Sweden 2025

Realistic Modelling of Li-ion Batteries for Calculating High Frequency Impedance
ADITHYA SIVAKUMAR
SURESH CHANDER DURAIVEL

Supervisor:
Dr.Raik Orbay,
Department of Strategy and Program Execution, Volvo Cars Corporation

Co-Supervisor:
Divyaraj Gadhavi,
Department of Strategy and Program Execution, Volvo Cars Corporation

Academic Supervisor/Examiner:
Dr.Torbjörn Thiringer,
Department of Electrical Engineering, Chalmers University of Technology

Master's Thesis 2025
Department of Electrical Engineering
Division of Electric Power Engineering
Chalmers University of Technology
SE-412 96 Gothenburg
Telephone +46 31 772 1000

Cover:

Typeset in LaTeX
Printed by Chalmers Reproservice
Gothenburg, Sweden 2025

Realistic Modelling of Li-ion Batteries for Calculating High Frequency Impedance.
Adithya Sivakumar
Suresh Chander Duraivel
Department of Electrical Engineering
Division of Electric Power Engineering
Chalmers University of Technology

Abstract

This thesis primarily focuses on building a robust 3-D simulation model and implementing a versatile solver setup for a Lithium-ion (Li-ion) battery cell to study the High-Frequency (HF) behavior. Although this study primarily focuses on the impedance characteristics of battery cells, it also investigates their multidisciplinary behavior, including electromagnetic, thermal, and structural aspects. The developed simulation model is initially validated using a simple copper wire and a coin cell battery before being applied on the cylindrical cell model. The 3-D model includes all cell layers with defined dimensions and tolerances, and is finely meshed in critical regions to ensure convergence and analyze mesh dependency.

The primary outcome of this study is the impedance as a function of frequency, swept across a range from 100 Hz to 100 MHz. The simulated data is compared with experimental test data of the same cell. This comparison helps understand the accuracy of the solver and study possible failure points. Another key outcome of this study is the development of a genetic algorithm (GA)-based computational framework designed to identify optimal solutions for cell design. This helps in balancing multiple user-defined objectives to achieve an efficient design solution with balanced trade-off among competing objectives.

The conclusion of the thesis is that a 3-D simulation model gives a better estimation of the real-world HF behavior, than a 1-D model which has numerous assumptions on the material behavior and field propagation. The studied Li-ion cell indicates a drop in impedance behavior in the mid-frequency range, attributed to dominant capacitive and resistive effects. At higher frequencies, beyond the cutoff frequency, an increase in impedance is observed due to dominant inductive behavior. This model is used to visualize field propagation and can be further scaled to the module or pack level to analyze and improve the EMC performance of the system. However, with further modifications, the developed simulation model can be better optimized for detailed analysis of multidisciplinary parameters such as temperature, Joule heating, displacement, and stress.

Keywords: 3-D, Battery cell, EMC, FEM, Genetic Algorithm, High-Frequency, Impedance, Li-ion, Multidisciplinary

Acknowledgments

This thesis was carried out in collaboration between Volvo Cars Corporation and the Department of Electrical Engineering at Chalmers University of Technology.

We would like to thank our Chalmers examiner, Prof.Torbjörn Thiringer, for providing us with the opportunity to work with this project and taking time out of his schedule to help us in providing his expertise and the necessary laboratory equipments.

We want to express our sincere gratitude to Dr.Raik Orbay & Mr.Divyaraj Gadhavi for their invaluable guidance throughout the master thesis. We are grateful for the time they have spent with us and their valuable inputs.

We would like to thank our manager at VCC, Mr.Anoop Suryanarayana for his support along the course of the thesis. We also would like to thank Mr.Daniel Karlsson for providing the preliminary CAD model to begin the thesis work. We thank Mr.Stephan Esteki for acquiring the X-ray tomography and Mr.Jonas Björkholtz for his help with the welding of the battery cell terminals.

We are also grateful to Mr.Aditya Singh, Mr.Johannes Emilsson and everyone at the 97100 Strategy and Program Execution department for all the helpful discussions along the course of the thesis.

Finally, we are indebted to our family and friends for motivating us throughout the master's degree. Their support and encouragement have been a constant source of strength during this journey.

Adithya Sivakumar, Göteborg,2025
Suresh Chander Duraivel, Göteborg,2025

Acronyms

Below is the list of acronyms that have been used throughout this thesis listed in alphabetical order:

1D	One Dimensional
3D	Three Dimensional
CAD	Computer-Aided Design
CO_2	Carbon dioxide
DC	Direct current
DUT	Device Under Test
EA	Evolutionary Algorithms
ECMs	Equivalent Circuit Models
EIS	Electrochemical Impedance Spectroscopy
EMC	Electromagnetic Compatibility
EMI	Electromagnetic Interference
FEM	Finite Element Method
GA	Genetic Algorithm
HF	High-Frequency
HPC	High-Performance Computing
HTC	Heat Transfer Coefficient
HV	High Voltage
KPI	Key Performance Indicators
LLMs	Large Language Models
LPMs	Lumped Parameter Models
MOGA	Multi-Objective Genetic Algorithm
MPI	Message Passing Interface
OEM	Original Equipment Manufacturer
PDE	Partial Differential Equations
SOGA	Single-Objective Genetic Algorithm
SOH	State of Health
SPD	Symmetric Positive Definite
VNA	Vector Network Analyzer

Contents

Chapter 1

Preface

Volvo Car Corporation (VCC) has been a front-runner in sustainable development within the mobility industry. Over the decades, the company has introduced numerous inventions that have advanced automotive technology. Volvo has become synonymous with safety, pioneering several groundbreaking safety features that have set standards for the industry. Founded in 1927 with the mission of making Swedish roads safer, VCC has grown into a global company that, as it approaches its centenary, continues to lead with a strong focus on safety, sustainability, and innovation.

1.1 Cutting-Edge Technologies

VCC has introduced numerous innovative technologies over the past years. Some of their pathbreaking inventions are

- The three point safety belt introduced in 1959.
- The rear facing child seat introduced in 1972.
- The Side Impact Protection System (SIPS) introduced in 1991.
- The Blind Spot information system introduced in 2003.
- Driver Understanding system introduced in 2023.

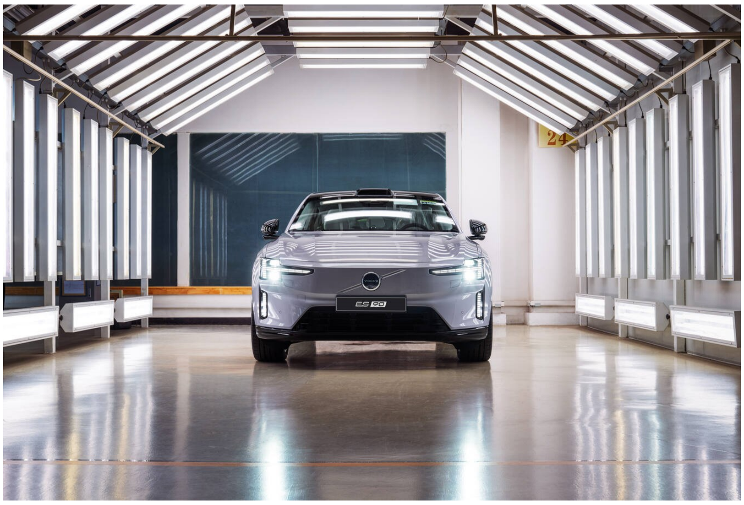

Figure 1.1: Volvo ES90: Volvo's latest premium electric car

1.2 Sustainable Mobility

Today, the challenges facing the automotive industry extend far beyond road safety. Climate change, global warming, CO_2 emissions and the depletion of natural resources are reshaping the expectations placed on manufacturers and pushing the industry toward electrification. This creates the need for highly efficient electric drivelines and vehicles. For Volvo Cars, this transformation is not just a technological shift but also strategic. The company aims to have electrified cars account for 90–100% of its global sales volume by 2030 and to achieve climate neutrality across its entire value chain by 2040 [1].

This thesis work is in alignment with Volvo Cars electrification targets and sustainability goals. In this work, a 3D finite element method (FEM)-based model of a Li-ion battery cell is developed to study its high-frequency behavior, which helps identify design inefficiencies and contributes to optimized material usage and improved energy efficiency of the cell. Additionally, a computational pipeline using genetic algorithm (GA) is developed to identify optimal solutions more efficiently with fewer iterations, which in turn accelerates the design process. This approach minimizes the need for physical prototyping, thereby significantly reducing energy consumption and carbon footprint, and directly contributing to sustainable product development in electrification.

Chapter 2

Introduction

2.1 Background

Sustainability is the main focus in the current global landscape. With industries across different domains pushing towards sustainable development, electrification is the present and future of the automotive industry. The demand for highly efficient hybrid and electric vehicles (xEV) has increased significantly. All automobile manufacturers are competing to be the most energy efficient in the market. The amount of energy in the car is limited by the battery capacity and it is therefore important to focus on the efficiency and battery life thereby reducing the carbon dioxide (CO_2) budget. The EU sustainability guidelines [2] has imposed stringent requirements on the production and usage of battery technology and hence significant technological advancements have been achieved in battery research. Several factors influence battery state of health (SoH) and performance, including direct current (DC) fast charging. Alternatives for DC fast charging, like high-frequency (HF) pulse charging [3] are being investigated due to the reduced impact on battery life and enhanced performance.

The HF behavior of batteries is of concern, because this behavior immediately affects the electromagnetic compatibility (EMC) of the system. Understanding the impedance behavior of battery cells at HF is crucial to minimize electromagnetic interactions and use effective electromagnetic interference (EMI) suppression techniques for the operating frequency range. This requires understanding the behavior of batteries and other electromagnetic systems in the operating conditions. Virtual models and simulation techniques are the ideal way to forecast the behavior of a subject without having to prototype a new version for every change. Virtual models cut down costs and strenuous lead times in terms of production and testing. This method helps in effectively capturing the physics inside the cell while having a accurate geometric detail. Hence this creates the need for detailed 3D models that can accurately estimate the electro-magnetic behavior especially at higher frequencies to mitigate the afore-mentioned issues.

2.2 Literature study

Impedance is usually modeled as network of resistors and capacitors [4]. Previously electrical study of battery cell has been done using equivalent circuit models (ECMs), Although ECMs are highly efficient, they simplify the electrochemical behavior of the cells. To address this, Yang et al. [5] proposed fractional-order ECMs with improved diffusion representation. Lumped parameter models (LPMs) are another option to study the electrical behaviour of cells, LPMs reduce complex Partial differential equations (PDE) to compact forms and account for the diffusion effects of a cell.

Tavares et al. [6] applied LPMs to lithium polymer batteries and compared it with other ECM based models and found LPMs can include the diffusion effects giving a more realistic representation of the cell. Although LPMs are realistic, they do not account for the spatial variation of the cell parameters. Three-dimensional finite element models (FEM) can help better capture these spatial effects and anisotropy. Pan et al. [7] used FEM to simulate pouch cell deformation under impact, showing that critical mechanical responses require a fully coupled thermo-mechanical model. Wang et al. [8] proposed a FEM-based thermal model for cylindrical cells, validated against experiments, which resulted in non-uniform internal temperature distributions that LPMs cannot reproduce.

Pauschau et al. [3] explored HF pulse charging on lithium ion batteries and found that pulse charging allows faster charging while reducing the stress on electrodes. However HF pulses can influence the impedance of the cells and can cause non-uniform heating. This creates the necessity to study the HF behaviour of battery cells. Landinger et al. [9] studied the HF behavior of cells and concluded that the HF impedance is design-dependent, that is, geometry driven inductances and capacitances have a significant impact above 10 kHz and LPMs fail to effectively capture these parameters [10]. Keller's skin effect theory [11], Zhang & Lv's EMI suppression studies [12], and the RIFEL project [13] link HF impedance with EMC behaviour in packs and vehicles. Together, these studies show ECMs and LPMs as powerful but limited when addressing anisotropic variation of the models. Although FEM models are used in mechanical and thermal analysis, it has been used very little in studying the electrical behavior. This proves as the main motivation to proceed with modeling a fully coupled electromagnetic-thermal-mechanical battery simulation model and building a simulation framework.

2.3 Objective

This thesis work aims to:

- Build a complete 3D FEM simulation model for performance evaluation and optimization of battery cells at various frequencies. The aim is to analyze the model in electromagnetic, heat transfer and structural mechanics domains.
- Correlate the 3D model simulation data with the measured data in the HF region between 1kHz to 100 MHz.
- Characterize the cell impedance at high frequencies up to 100 MHz and inter-

pret the underlying causes for the observed behavior
- Model structural behavior to quantify the displacement and capture heat transfer phenomena to identify maximum temperature region in the cell.
- Analyze the magnetic field strength at different frequencies.
- Capture the computation time and scalability of the developed thermo-mechatronic model.
- Devise an effective computational pipeline for multidisciplinary design by balancing multiple objectives, with focus on a critical battery component.

2.4 Research questions

To achieve the stated objectives, this thesis addresses the following key research questions:
- How to use a 3D FEM model for studying high frequency multidisciplinary behavior of the battery cells?
- What is the accuracy of the 3D simulation model when validated against the experimental electrical behavior?
- What are the potential advantages and drawbacks of using the developed model for future study?

2.5 Limitations

The provided 3D computer-aided design (CAD) model of the battery cell does not precisely match the geometry of the physical cell. Due to model complexity and time constraints, only partial modifications were made to the CAD. Therefore, matching the simulation results against the experimental data is not completely feasible. Some of the material properties used in the simulations were not obtained from validated sources, and anisotropy in these properties was not considered due to lack of data availability. These limitations are addressed in detail during this study.

Chapter 3

Theory

This thesis work deals with the electrical elements of a battery cell like impedance, electromagnetism, etc. Impedance, Impedance estimation and measurement techniques are discussed in detail in this chapter. The fundamental principles governing the solvers used also also explained in detail. The software used in this research work- ElmerFEM, basics of meshing and mesh types are also discussed here.

3.1 Impedance

Impedance is a complex ratio of voltage and current in an AC circuit. It can also be defined as the resistance of a circuit at a particular frequency. It captures both resistive and reactive behavior of a circuit element and determines how a circuit responds to a time-varying signal.

$$Z = R + jX = \frac{\overline{V}}{\overline{I}} \tag{3.1}$$

where R=Re(Z) is the resistance and X=Im(Z) is the reactance. For a resistive element, the impedance is real and constant.

$$Z_R = R \tag{3.2}$$

For capacitive and inductive elements, the reactance varies with frequency.

$$Z_C = jX_C = \frac{1}{j\omega C} \quad ; \quad Z_L = jX_L = j\omega L = j \cdot (2 \cdot \pi \cdot f) \cdot L \tag{3.3}$$

Where X_C and X_L are the capacitive and inductive reactances, and L and C are the inductance and capacitance, respectively. ω is the angular frequency, L is the inductance and C is the capacitance respectively.

The electrical power losses of a system is

$$P = I^2 \cdot Z \tag{3.4}$$

Where P is the power loss in Watts, I is the current flowing through it, Z is the total impedance of the system [4].

3.1.1 Resistance

The resistance of a material is the opposing force of the material to charge flow through it. Theoretically, resistance of a material can be calculated by

$$R = \frac{\rho . l}{A} \tag{3.5}$$

where ρ is the resistivity of the material, l is the length of the conductor, and A is the cross-sectional area of the conductor.

The resistance of a material is determined by the following properties [4]:

- Material
- Length
- Temperature
- Cross sectional area

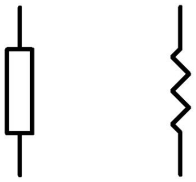

Figure 3.1: Resistance/Resistor *(Electrical representation of an resistor)*

3.1.2 Capacitance

Capacitance is a fundamental property of an electrical system that quantifies its ability to store electric charge per unit. Capacitance arises from the separation of charges within an electric field and is determined by the geometry of the conductors and the dielectric properties. The capacitance of a parallel-plate capacitor can be calculated as:

$$C = \frac{\epsilon_0 A_p}{d} \tag{3.6}$$

where ϵ is the absolute permittivity of the dielectric material, A_p is the area of the plates, and d is the separation distance [4].

Figure 3.2: Capacitor/Capacitance *(Electrical representation of an capacitor)*

3.1.3 Inductance

Inductance is a property of a conductor or circuit that defines the relationship between time-varying current and the magnetic vector potential it generates. It reflects a system's ability to store magnetic energy and oppose changes in current via self-induced Electromotive Force (EMF), also known as back-EMF [4].

$$v(t) = L\frac{di}{dt} \tag{3.7}$$

where $v(t)$ is the voltage as a function of time, L is the inductance of the material, i is the current, t is time and $\frac{di}{dt}$ is the time derivative of current.

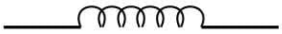

Figure 3.3: Inductor/Inductance *(Electrical representation of an inductor)*

3.2 Impedance of a battery cell

The impedance of a lithium-ion battery cell is a complex, frequency-dependent quantity. It characterizes the electrochemical system's resistance to the flow of alternating current. This encapsulates the combined effects of bulk material resistances, interfacial charge transfer processes, and double-layer and diffusion-related phenomena occurring within the cell. Impedance is mathematically expressed as

$$Z = X_R + jX_{\mathrm{im}}(\omega) \tag{3.8}$$

where ω is the angular frequency and $X_R + X_{Im}$ are the real and imaginary components that reflects resistive (ohmic) and reactive (capacitive and inductive) behaviors that vary with frequency. Low-frequency impedance responses typically reflect mass transport limitations and electrode kinetics, whereas high-frequency characteristics are governed by electronic/ionic conductivity, ohmic and contact resistances [10].

3.3 Impedance estimation methods

In impedance estimation methods, numerical models are built to estimate the impedance parameters, capture effective physical phenomena and study the behavior of the model. Simulation models are key to accurate estimation of the system behavior. A robust model defines the directional dependency & material dependency of the parameters. Modeling has two different approaches:

- Lumped parameter model
- Distributed parameter model

3.3.1 Lumped parameter model

A lumped-parameter model is a simplified mathematical representation of a physical system in which the anisotropic behavior of the state variables (e.g., temperature, voltage, displacement) are neglected. The dependent variables of interest are a function of time alone. The system is described by a finite number of ordinary differential equations (ODEs) [14].

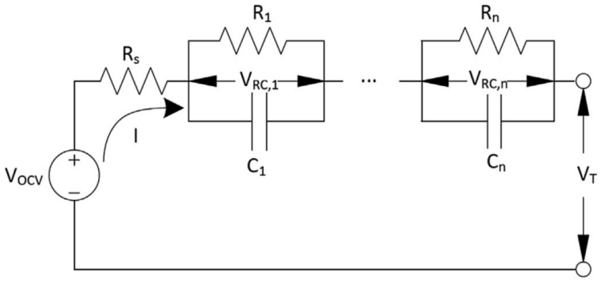

Figure 3.4: Lumped parameter model of a lithium Ion battery[5].

3.3.2 Distributed parameter model

A distributed parameter model accounts for the anisometric behavior of state variables within a system. Here, all dependent variables are functions of time and one or more spatial variables. In this case, the system is described by solving Partial Differential Equations (PDEs). The spatial resolution of all variables helps with better prediction, particularly under high current loads or non-uniform operating conditions, where localized heating and other gradients becomes significant [9].

3.4 Impedance measurement methods

Impedance measurement can be done by various different methods, some of them are listed here:

1. Bridge method
2. Vector Network Analyzer(VNA) method
3. Electrochemical Impedance Spectroscopy (EIS) method

Due to it's narrow frequency range, bridge method is not of interest for the scope of this study. We'll look into the other two methods in detail [15].

3.4.1 Vector Network Analyzer: VNA Method

The Vector Network Analyzer method is a versatile technique used to extract the impedance of Device Under Test (DUT) by various methods.

- Scattering parameter method: Electrical signals are transmitted and reflected through two ports and the DUT to measure the scattering parameters (S-parameters) and compute the impedance from it.

- Impedance adapter method: This method is only possible with the Bode 100, which is the test instrument used for the scope of this study. The DUT is tested in conjunction with a B-WIC or B-SMC and offers a wide measurement range. B-WIC (Wired Interface Connector) is the fixture used for through hole components and the B-SMC (Surface Mounted Connector) is a fixture used for surface mounted components [16].
- Shunt through method: Shunt through method is used for measuring very low impedance values, as it is sensitive for very low value measurements. This method emulates a Kelvin connection [17], where the input port drives a signal through the DUT and the other channel measures it.
- Series through method: Series through measurement is a similar measurement technique like shunt through, but is used to measure high impedance values.

Table 3.1: VNA Measurement Modes

Method	Measurement Range	Advantage
Impedance Adapter	20 mOhm to 600kOhm	Wide measurement range
Shunt through	1mOhm to 100 Ohm	Can measure very low impedances
Series through	1 KOhm to more than 1MOhm	Useful for measuring very high impedance values

3.4.2 Electrochemical Impedance Spectroscopy (EIS)

EIS is a widely used frequency domain technique for characterizing the dynamic behavior of electrochemical systems.This method is often used to measure the impedance of a system across a wide frequency range. By applying a sinusoidal voltage or current perturbation of a small amplitude over a range of frequencies and analyzing the linear response of the system, the EIS enables the resolution of various electrochemical phenomena occurring at different time intervals.This is a non-destructive method and is used extensively in areas such as battery diagnostics, corrosion analysis, fuel cell monitoring, and bio sensing [18].

The impedance Z(ω) is a complex function of angular frequency $\omega = 2\pi$f, defined as

$$Z(\omega) = \frac{V(\omega)}{I(\omega)} = X(\omega) + jY(\omega) \tag{3.9}$$

where X and Y represent the real (resistive) and imaginary (reactive) components of the impedance, respectively, and j is the imaginary unit. EIS measurements typically span a frequency range from megahertz to millihertz, enabling the analysis of fast charge transfer processes and slower diffusion-controlled mechanisms. Results are often represented using nyquist plots (imaginary vs real impedance) or Bode plots (magnitude and phase vs frequency), offering qualitative and quantitative insight into system behavior. Data is interpreted through equivalent circuit modeling, in which the system is represented by an electrical circuit composed of elements such as resistors, capacitors, constant phase elements (CPE) and Warburg impedance [19].

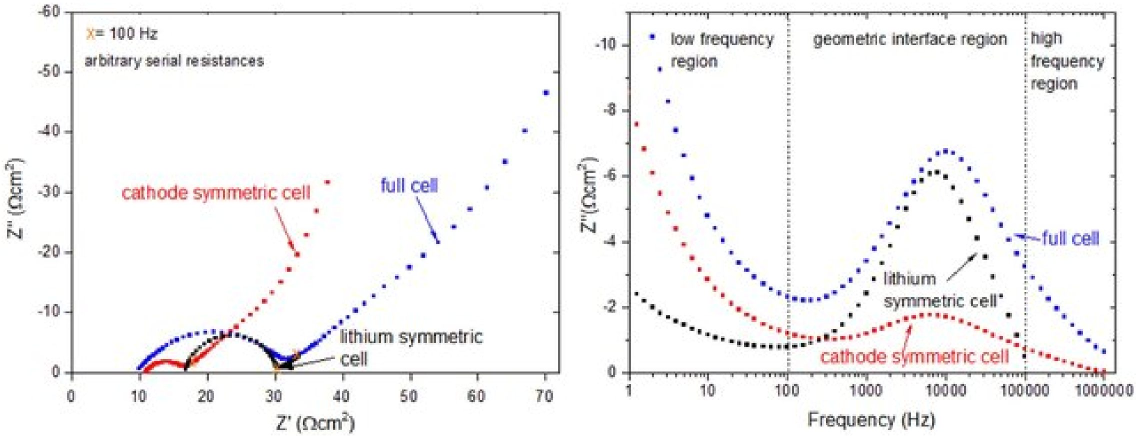

Figure 3.5: EIS & Bode plots of a lithium ion half cell and full cell [10]

The nyquist plot provides a comprehensive idea of the cell behavior and various electrochemical and bulk phenomena that occur at different frequency ranges. From Figure 3.6 we can see that at higher frequencies (>1kHz), the ohmic effects and inductive tail of the cell are dominant. At mid frequencies (<1kHz to 0.1Hz), the electrolytic effects and the charge transfer process are dominant. At low frequencies (<0.1Hz), the diffusion effects of the battery cell show an effect [20].

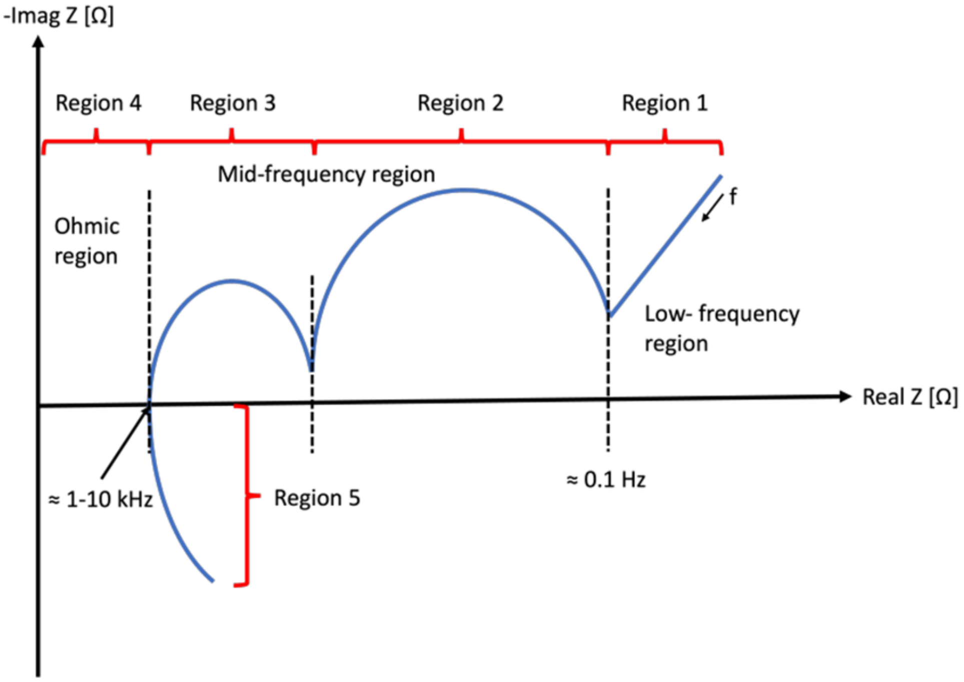

Figure 3.6: Nyquist plot of a lithium ion cell [10]

The bode plot is used to study the behavior of the DUT in different frequencies. The magnitude and phase angle are plotted against the frequency in logarithmic scale. The magnitude plot, plotted in ohms, shows the cell's resistive and reactive contributions throughout the frequency spectrum, while the phase plot, expressed in degrees, shows the relative dominance of capacitive and inductive behaviors in different electrochemical processes [13].

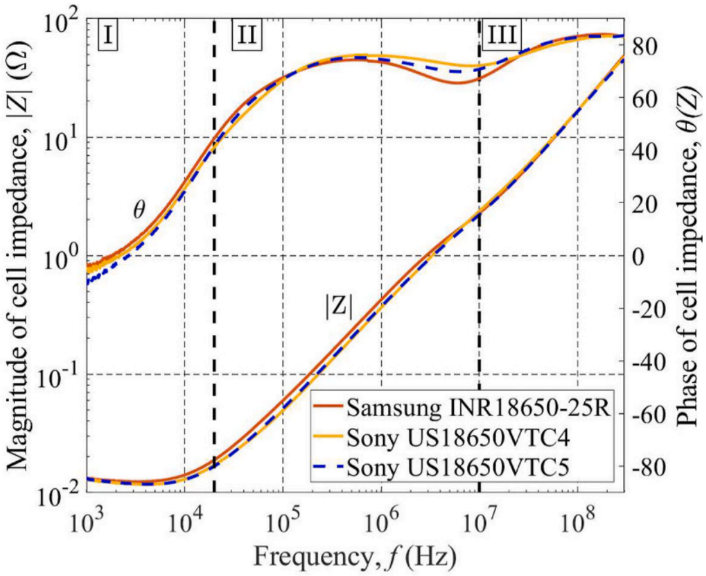

Figure 3.7: Bode plot comparison of cylindrical cells [9]

3.5 Electromagnetic theory

The electromagnetic behavior of any body can be defined by a set of partial differential equations commonly known as Maxwell's equations. The equations (3.10)-(3.13) describe the relationships between electric fields, magnetic fields, electric charge density, and electric current density in both free space and material medium [13].

Maxwell's first equation is also known as Gauss's law of electricity, which states that the divergence of the electric field is proportional to the charge density. In simpler words, electric charges act as sources (or sinks) of the electric field [21]. It is expressed as,

$$\nabla \cdot \mathbf{E} = \frac{\rho}{\epsilon_0} \tag{3.10}$$

where E is the electric field, ρ is the electric charge density and ϵ_0 is the permittivity of free space.

The second equation of Maxwell is known as Gauss's Law of Magnetism. It states that the divergence of magnetic flux density is zero. It means magnetic monopoles do not exist and magnetic field lines always form closed loops [21].

$$\nabla \cdot \mathbf{B} = 0 \tag{3.11}$$

where B is the magnetic field.

Faraday's law states that change in magnetic flux over time induces a non-conservative electric field.In other words, this law reflects how electric and magnetic fields transform into each another under changing reference frames [21].

$$\nabla \times \mathbf{E} = -\frac{\partial \mathbf{B}}{\partial t} \tag{3.12}$$

Maxwell's fourth equation generalizes Ampère's circuital law by including the displacement current term, $\mu_0 \varepsilon_0 \frac{\partial \mathbf{E}}{\partial t}$. The displacement current term also allows for the self-sustaining propagation of electromagnetic waves in free space, with oscillating electric and magnetic fields continuously regenerating each other [21]

$$\nabla \times \mathbf{B} = \mu_0 \mathbf{J} + \mu_0 \epsilon_0 \frac{\partial \mathbf{E}}{\partial t} \tag{3.13}$$

where μ_0 is the vacuum permeability and J is the current density.

Skin effect in a conductor

AC current through any conductor gives rise to skin effect in it. The skin effect is an electromagnetic phenomenon in which an alternating current preferentially flows along the outer surface of a conductor, rather than uniformly through its crosssection. The current density, J_d, decreases exponentially with skin depth δ into the conductor based on the equation [11]:

$$|J_d| = |J_0| \cdot e^{-\frac{d}{\delta}} \tag{3.14}$$

where J_0 is the surface current density of the conductor in A/m^2 and d is the distance from the conductor's surface in meters.

The skin depth δ is a frequency dependent parameter, which is inversely proportional to frequency

$$\delta = \frac{1}{\alpha} = \frac{1}{\omega . f(\epsilon, \mu)} \tag{3.15}$$

where ϵ and μ are permittivity and permeability respectively and $f(\epsilon, \mu)$ is a function of permittivity and permeability.

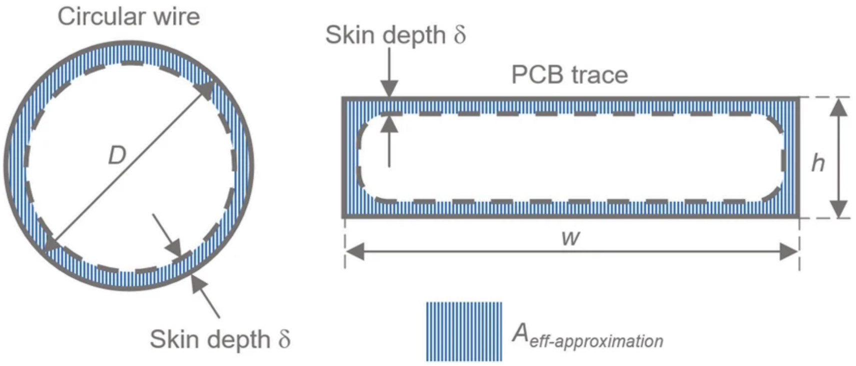

Figure 3.8: Skin effect in a conductor [11]

3.6 Heat transfer theory

The thermal behavior of a battery cell is both internal and external by nature.

- **External modes of heat transfer**
  - **Conduction**: Energy transfer through molecular vibration. It follows the Fourier's law of conduction [22].

    $$q = -k\frac{dT}{dx} \tag{3.16}$$

    where q is the heat flux in W/m^2, k is the thermal conductivity in (W/mK) and T is the temperature of the object in K.

  - **Convection:** Energy transfer through bulk fluid motion. Convection obeys Newton's law of cooling [22].

    $$\frac{dT}{dt} = -h(T - T_{\text{env}}) \tag{3.17}$$

    where T_{env} is the ambient temperature,h denotes the heat transfer coefficient (HTC), expressed in units s^{-1}.

  - **Radiation:** Energy transfer through the emission, propagation and absorption of electromagnetic waves generated by charged particles within the body. It follows Stefan-Boltzmann's law of radiation [22].

    $$E = \sigma T_b^4 \tag{3.18}$$

    where E is the Radiant emittance of a blackbody (W/m^2), σ is the Stefan-Boltzmann constant, T_b is the absolute temperature of the body (K).

- **Internal heat generation:**
  - **Joule Heating:** The irreversible conversion of electrical energy into thermal energy within a conductive medium is known Joule heating/Ohmic heating. It occurs due to the dissipation of current in the body due to it's electrical resistance [21].

    $$q_v = \mathbf{J} \cdot \mathbf{E} = \sigma E^2 = \frac{J^2}{\sigma}, \tag{3.19}$$

where q_v is the volumetric heat generation rate (W/m^3), J is the current density in (A/m^2),E is the electric field vector (V/m), and σ is the electrical conductivity in (S/m).

3.7 Theory of elasticity

Any material undergoes both reversible and irreversible deformation/displacement based on the stress and strain acting on the material. Linear elasticity defines how elastic objects undergo reversible deformation proportional to the applied load [23]. It is characterized by the linear stress-strain relation defined by Hooke's law. The dynamic equation for elastic deformation of solids is given by

$$\rho \frac{\partial^2 \vec{d}}{\partial t^2} - \nabla \cdot \tau = \vec{f} \tag{3.20}$$

where ρ is the mass density of the material (kg/m^3), $\vec{d}$ is the displacement vector (m), $\frac{\partial^2 \vec{d}}{\partial t^2}$ is the material acceleration (m/s^2). τ is the Cauchy stress (Pa) and $\vec{f}$ is the body force vector per unit volume.

This elastic deformation includes external loads applied to the body as well as thermal loads and displacements due to lorentz forces acting internally and causing an effect [23].

3.8 ElmerFEM

ElmerFEM [24] is an opensource multiphysical simulation software, that supports parallel computing and has physical models of fluid dynamics, structural mechanics, electromagnetics, heat transfer and acoustics and more.

Elmer offers flexibility in choosing multiple solvers/modules at once and solving across multiple disciplines. The following are some features that elmer offers to the user for better approximation.

- **Iterative method**: Iterative methods in ElmerFEM refer to a set of numerical algorithms used to solve the finite element discretizations of PDE's.

  Unlike direct solvers, which compute the solution vector through matrix factorization, iterative methods generate a sequence of approximate solutions starting with an initial guess, refining the estimate until a predefined convergence criterion is satisfied. Some of the iterative methods available in ElmerFEM are CG, BiCGStab, GMRES [25].
- **Convergence tolerance**: Convergence tolerance is a user-defined parameter that specifies the allowable relative or absolute error between successive approximations in an iterative solver. This factor governs the stopping criterion for solving a system in Elmer [25].

- **System preconditioning**: System preconditioning is a numerical technique applied to improve the convergence properties of iterative solvers by transforming the original system of equations into another equivalent form [25].

  Common preconditioning strategies available in ElmerFEM include diagonal scaling (Jacobi), ILU factorization, incomplete Cholesky (IC), The choice of preconditioner significantly affects both the rate of convergence and the total computational cost of solving large-scale finite element systems. Proper selection and tuning of the preconditioner is essential for efficiently solving computationally intensive simulations in structural mechanics, heat transfer, or fluid dynamics [25].

For electromagnetics, we have

- **Electrostatic solver**: This solvers uses the electromagnetic theory (Maxwell's equations) to compute the electrostatic potential in a conducting medium.
- **Static current solver**: This module derives the volume current and losses in a conducting medium by solving for the electrostatic potential similar to the previous solver.
- **Magnetodynamics**: This module solves a version of the maxwell's equations in the A-V form. This can be used to compute in time domain as well as frequency domain [25].

There are also solvers for computing Electromagnetic (EM) waves, magnetic induction, etc.,

For heat transfer

- **Heat equation**: This module follows the energy conservation principle and Fourier's law is used to model the heat conduction, frictional heating and joule heating is also solved in this module [25].

For elasticity and displacement computation

- **Linear elasticity**: This module computes the displacement field from the elastic deformation of solids. Thermal stresses may also be solved in post processing [25].

3.9 Meshing for FEM

In FEM, a mesh refers to the discretization of a continuous geometric domain into a finite elements. This is used to approximate field variables over the domain. Each element is defined by a set of nodes and is associated with interpolation functions (shape functions) that represent the variation of the solution within the element. The mesh transforms the partial differential equations that govern physical phenomena such as stress, heat transfer, or fluid flow into a system of algebraic equations that can be solved by numerical techniques [26].

3.9.1 Types of meshes based on mesh generation techniques

- **Structured mesh**: A collection of hexahedral elements with implicit connectivity between the mesh points is called a structured mesh. Depending on the geometry, it may be necessary to manually divide the domain into multiple blocks, making the process of creating structured meshes for complex geometries time consuming [27].
- **Unstructured mesh**: A set of elements, usually tetrahedrons (tetra), that have an explicitly defined connectivity is called an unstructured mesh. The creation of points and the definition of the connectivity between them are the two fundamental elements in the mesh generation process. Though unstructured mesh might be a better choice due to it's flexibility in mesh generation, the solution accuracy maybe less than that of the structured mesh due to the existence of skewed elements in sensitive regions such as boundary layers [27].
- **Hybrid mesh**: Hybrid mesh is usually a combination of hexahedral elements in the critical and boundary layers of the domain and tetrahedral elements in the rest of the domain [27].

3.9.2 Types of meshes in ANSA

ANSA [28] is an interdisciplinary CAE pre-processing tool that offers all the features required for full-model build-up in a single integrated environment, from CAD model to an input file ready to run the solver. ANSA is used to do geometric modifications and do refined meshing. ANSA offers flexibility in terms of it's wide range of features and tools.

The types of meshes in ANSA are

- **Surface Mesh**: The 2D mesh that is done on the surfaces of the model is called the surface mesh. ANSA offers a lot of features like edit, cut, mark and move the node elements in the mesh.

  The following are the types of surface mesh elements:
  - Quad: Quadrilateral element (4-sided element)
  - Tria: Triangular element (3-sided element)
  - Ortho-Tria: Orthogonal triangular element (triangular element with near-orthogonal angles)
  - Mixed: A combination of quadrilateral and triangular elements

- **Volume Mesh**: After the surface mesh is done, meshes are done in 3D volumes of the model. This is known as volume mesh. The volumes are detected in the model and meshed.

  The following are the types of volume mesh elements:
  - Tetra-FEM: Tetrahedral mesh (composed of 4-node or higher-order tetrahedral elements).
  - Tetra Rapid: Rapid Tetrahedral Mesh (Faster, less computationally intensive version of tetrahedral mesh).

  - HexaPoly: Hexahedral-Polyhedral mesh consisting mainly of hexahedral elements (and sometimes polyhedra). This offers better numerical accuracy and stability compared to tetrahedral mesh.
  - Hexa Interior: Structured hexahedral elements in the interior combined with tetrahedral or polyhedral elements at the boundaries).

3.10 Evolutionary algorithms for multiphysics KPI balancing

Evolutionary Algorithms (EAs) are population-based optimization methods from the AI toolbox [29]. In a broader perspective, they develop a population of candidate solutions through iterative process of evaluation, selection and variation. EAs are particularly effective in multiphysics studies, where design involves interaction of several physical models (e.g. electromagnetic, thermal and structural) that are complex, non-linear, and computationally expensive. Unlike gradient-based optimization methods, EAs are derivative-free, enabling robust exploration of complex design spaces while capturing trade-offs among competing objectives.

3.10.1 Genetic Algorithm (GA)

Among the EAs, genetic algorithm is one of the most widely applied methods [30]. They are often suitable in multiphysics studies because they can handle discrete, continuous, and mixed variables, and they are naturally extendable to multi-objective optimization framework. Compared to other EAs such as particle swarm optimization or differential evolution, GAs are preferred because of their balance between exploration (global search) and exploitation (refinement).

3.10.1.1 Genetic algorithm parameters and definitions

Some general notable definitions for the optimization study are [31]:

- Individual: Refers to one complete candidate solution for the problem.
- Population: A collection of these individuals.
- Parents: An existing solutions from the current population
- Offspring: New candidate solutions produced from parents.
- Gene: A single decision variable inside the solution.
- Mutation: Refers to the probability that each variable randomly changes.
- Reproduction: Process of generating new candidate solutions using crossover and mutation.

Definitions for the control parameters that govern the GA are described [31] [32]:

1. Population & evaluation parameters
    - Population size: Number of solutions per generation.
    - Maximum function evaluations: Stopping criteria for the solutions.
2. Initialization
    - Initialization type: How the initial set of population is generated.

3. Crossover (recombination)
    - Crossover type: Determines how parent solutions are combined to generate offspring.
    - Number of offspring: Specifies how many candidate solutions are produced from a given pair of parents.
    - Crossover rate: Probability with which genetic material from selected parents is recombined to produce offspring during reproduction.
4. Mutation parameters
    - Mutation type: Decides how the random changes are applied.
    - Mutation rate: Probability each gene mutates.
5. Fitness parameters
    - Fitness type: Decides how the solutions are ranked in pareto front.
    - Replacement type: How solutions survive into the next generation.
6. Niching & shrinkage parameters
    - Shrinkage percentage: Minimum fraction of the population that survives.
    - Niching type: Decides the minimum spacing in the objective space.
    - Post-processor type: Secondary spacing mechanism to ensure diversity.

3.10.1.2 Key Operators in genetic algorithm

The search process in GA is driven by following operators [31]:

- **Initialization:** The algorithm begins by generating population of candidate solutions.
- **Crossover:** New solutions are generated by combining parts of parent solutions. This allows promising features from different solutions to be inherited by offspring.
- **Mutation:** Random modifications are introduced into solutions. This help maintain diversity and prevent premature convergence to local optima.
- **Niching:** Determines the distribution of the candidates across the objective space, preventing the population from clustering in Pareto front.

Chapter 4

Methodology

This section details the methodology employed throughout the thesis. It includes model building in ANSA [28] (includes geometric updates and mesh generation) and analysis in ElmerFEM [24] (including materials, governing equations, solver configurations, boundary conditions and other relevant inputs). In addition, the design and implementation of the experimental setup are presented. Figure 4.1 presents a flowchart that provides a comprehensive overview of the methodology used during this thesis work.

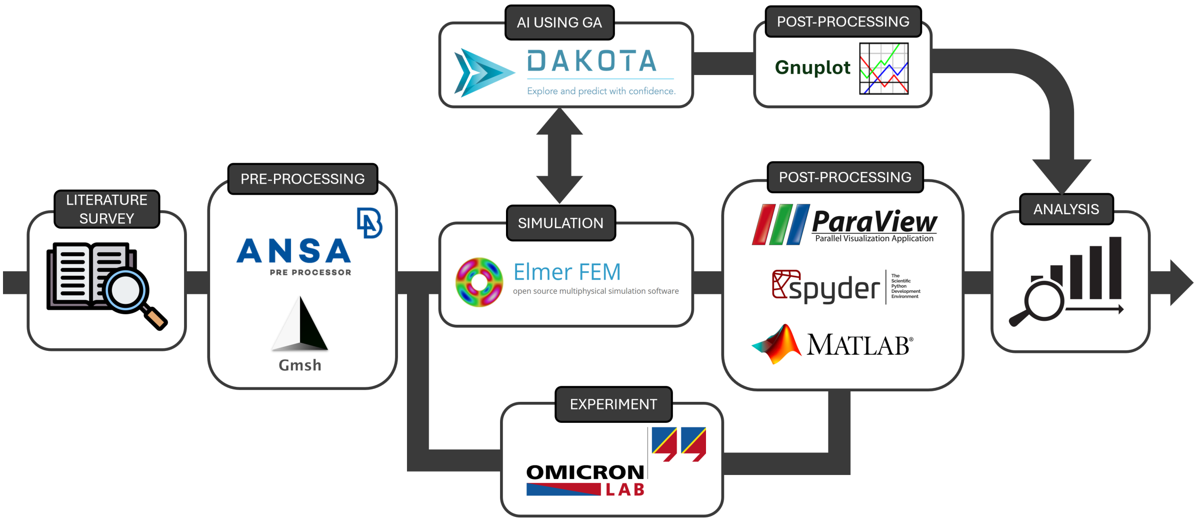

Figure 4.1: Overview of the thesis methodology

The first step for this thesis is to understand similar studies for the battery cell simulations from the literature as discussed in Chapter 2. After learning from the literature, the given battery cell model is modified and meshed using ANSA preprocessor and Gmsh tool [33].

Following this the fundamental principles from multiple disciplines are studied while the solver scripts are developed in ElmerFEM. These include electromagnetism (such as Maxwell's equations), heat transfer (such as Fourier's law of heat transfer), and structural mechanics (such as the Navier equations) as discussed in Chapter 3.

The ElmerFEM simulation are run using the High-Performance Computing (HPC) cluster network in Linux operating system. Additionally, Message Passing Interface (MPI) is used for parallelization of the simulation. Simultaneously the experiments were conducted using OMICRON Lab's VNA [34]. The experimental data is logged using Bode Analyzer Suite software tool. For post processing, the graphical representation of the results are obtained using Spyder IDE (python language) [35] and MATLAB [36]. The 3-D visualization of the simulation results are analyzed using ParaView [37]. Genetic algorithm is implemented with the help of python scripts through Dakota [38] and Gnuplot [39] is used for plotting.

There are two case studies considered before the cylindrical cell simulation is performed as shown in Figure 4.2. While developing the solver script, a simple wire model is simulated to verify the solver and its configurations. The measurements from an actual wire are taken and compared to validate the simulation results. Following that a sample coin cell model is simulated to check if the impedance behavior and field vectors of the cell are as expected. For this study, the frequency range is defined based on the literature as discussed in Section 3.4.2

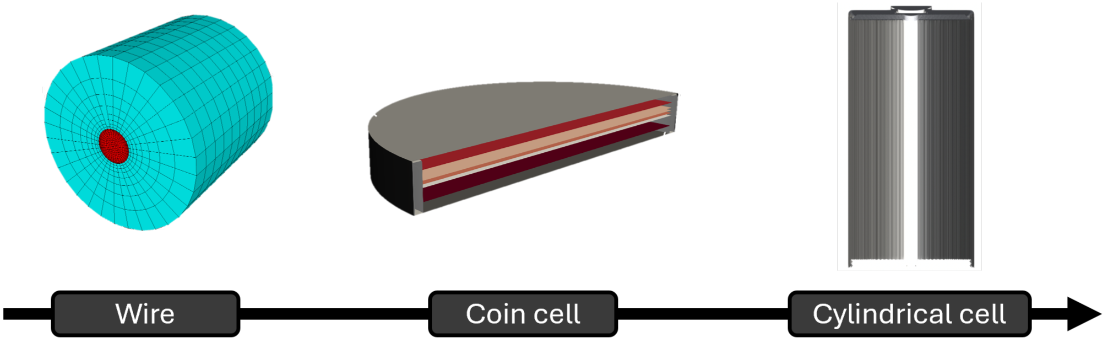

Figure 4.2: Selected case study models for simulation

4.1 Solver Description

The most important solver modules implemented from ElmerFEM are the MagnetoDynamics, HeatSolver and StressSolver [25]. These are used to compute the magnetic field, electric field, joule heating and temperature based on the body forces, initial conditions and boundary conditions applied on the cell components. The governing equations used in these solvers are explained in section 3.5, 3.6 and 3.7. The other solvers implemented are ResultOutputSolve and SaveData which are used to visualize the output and extract data points for the different variables.

4.1.1 Magnetodynamics

The WhitneyAVSolver for the magnetodynamics is the primary electromagnetic solver that computes Maxwell's equations in the A-V form using edge finite element basis functions for the vector potential and Lagrange interpolation for the scalar potential. It supports both time-domain and frequency-domain computations with additional solvers for nodal and element wise approximation of derived fields. In this study, all computations were performed predominantly using frequency-domain simulation.

As a post-processing solver, the MagnetoDynamicsCalcFields computes derived fields such as joule heating, current density, and electric fields using the A-field (magnetic vector potential) obtained from the WhitneyAVSolver. The nodal forces are also computed in the post-processing solver. The estimated nodal forces are due to the mechanical force resulting from electromagnetic fields, typically Lorentz forces and Maxwell stress effects acting on the bodies.

4.1.2 Heat solver

The HeatSolve solver computes heat conduction using Fourier's law and heat equation incorporating energy conservation. The temperature is the primary field computed, while the other derived thermal fields such as heat flux vector and thermal energy density can also be computed. Since joule heating is computed by the MagnetoDynamics solver, the resulting heat generation is incorporated in the heat equation as an input for the temperature computation. This coupling ensures that the resistive heating effects are properly accounted, thereby providing a realistic representation of the multiphysics behavior.

4.1.3 Stress solver

The StressSolve module primarily computes displacement fields using Navier equations of elasticity. In addition to the displacement field, the solver is capable of estimating the other mechanical fields such as stress and strain tensors, von Mises stress, principal stresses, and principal strains. Furthermore, energy-related quantities such as the strain energy density can also be computed. The nodal forces computed by MagnetoDynamicsCalcFields solver are applied as body forces thereby allowing the stress solver to account for the force field from magnetic simulation for displacement computation. Therefore, the deformation behavior and failure points of the materials can be analyzed using this solver. It also supports the usage of anisotropic material properties.

4.1.4 Solver configurations

The Table 4.1 illustrates the notable configurations of the chosen solver parameters in ElmerFEM. In this section, the parameters that are modified to enhance the solver outputs are discussed, whereas the default configurations are maintained for the remaining solver parameters.

Table 4.1: Configured parameters used in ElmerFEM solvers

Parameters	**MagnetoDynamics solver**	**HeatSolve solver**	**StressSolve solver**
Iterative method	BiCGStab	BiCGStab	BiCGStabl
Convergence tolerance	1.0e-6	1.0e-6	1.0e-6
System preconditioning	Not used	ILU(0)	Not used

The reasoning for the selection of the iterative method is discussed in upcoming section 4.1.4.1. The convergence tolerance for all solvers is determined through an iterative approach. A preconditioner is employed when the iterative solver exhibits slow convergence or fails to converge. In this study, HeatSolve solver was observed to have slow convergence therefore, a basic ILU(0) preconditioner is introduced. The use of ILU(0) not only improved the convergence rate but also consumed minimal additional memory.

4.1.4.1 Linear system iterative method

The most commonly used iterative methods options available in ElmerFEM are studied. The key differences and use cases referenced from the ElmerSolver manual [40] are summarized in Table 4.2. Based on several iterations and the available data, it is evident that BiCGStab and GMRES iterative methods exhibit smoother convergence. However, considering the computational memory and simulation time, the BiCGStab method has been selected for use in all solvers used in this study.

Table 4.2: Different types of linear system iterative methods in ElmerFEM solver

Iterative method	Memory usage	Note
CG	Low	Very fast, simple and only for SPD systems
BiCGStab	Low	Fast, moderate stability and better convergence than CG
BiCGStab(l)	Moderate	Fast and higher stability than BiCGStab
GMRES	High	Memory-intensive (slow), very high stability and convergence

4.2 Harmonic wire model set-up

This particular case is a simple copper wire in a far field, with wire diameter D = 0.75 mm, where a potential is applied to induce a harmonic current. This model is adapted from tutorial 14 of the Elmer GUI Tutorials documentation [41] and modified to match the chosen wire. This case study is used due to the simplicity of the model, thus allows us to validate the solver outputs and impedance estimation. After the simulation, the induced current density and impedance magnitude outputs from the solver are validated with analytical calculations.

The materials assigned to the wire and far field are copper and air respectively. Material property values are critical inputs that are applied on the virtual model to ensure that its behavior closely approximates that of the real material. These values are taken from Elmer material library [24] and are presented in Table 4.3.

Table 4.3: Material properties for the wire model

Property	**Copper**	**Air**
Density (kg/m^3)	8960	1.205
Heat Capacity (J/kg·K)	385.0	1005.0
Relative Permeability	0.999994	1.00000037
Electric Conductivity (S/m)	59.59×10^6	1×10^{-13}
Sound Speed (m/s)	3810.0	343.0
Heat Expansion Coefficient (1/K)	16.5×10^{-6}	3.43×10^{-3}
Heat Conductivity (W/m·K)	401.0	2.57×10^{-2}
Young's Modulus (Pa)	115×10^9	N/A
Poisson Ratio	0.34	N/A
Relative Permittivity	1.0	1.00059

4.2.1 Meshing

The mesh generation script 'wire.grd' from the tutorial is modified and used to generate mesh for this study. This creates a coarse mesh for far-field and comparatively finer mesh for the wire as shown in wire mesh geometry (Figure 4.3). Mesh levels refers to the number of times the original mesh is subdivide into more mesh elements inside ElmerFEM. The original wire model has 5760 mesh elements. For this case a mesh level of 2 is used as default for all simulations to increase the mesh elements in the simulation. This is done to capture parametric gradients more accurately. Number of mesh elements from mesh level 2 in the wire model is 11520.

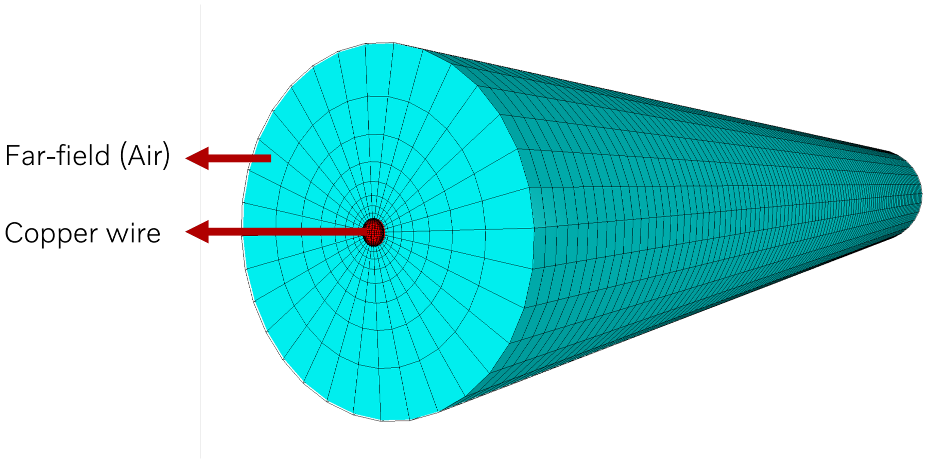

Figure 4.3: Wire mesh geometry

4.2.2 Boundary Conditions

The following are the boundary conditions applied to the bodies (Figure 4.4) :

- A Voltage of 1 V is applied at the inlet and ground of 0 V at the outlet.
- Initial condition for all bodies are set to room temperature (300 K).
- Joule heating is taken as a body force, thus the heat generated during current

flow is considered as a heat source. This propagates in the solution domain using heat transfer equation.

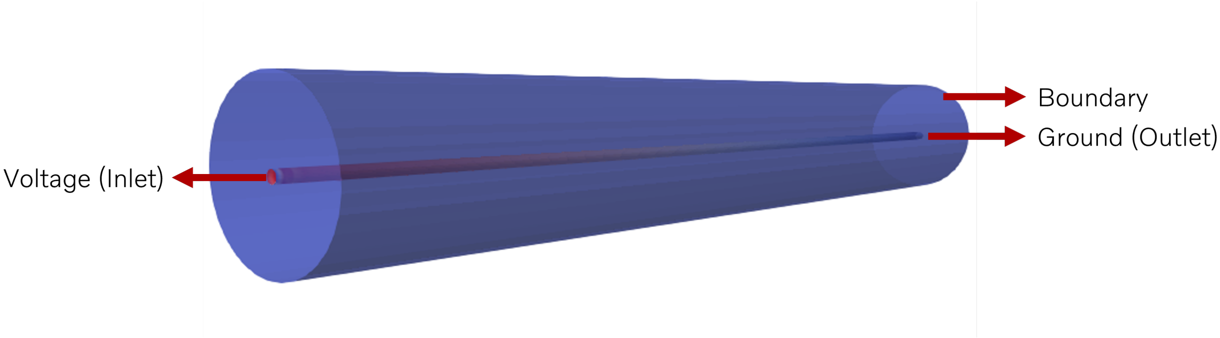

Figure 4.4: Wire model boundary condition

4.2.3 Wire Case study

Wire case 1: A steady state simulation is run for the applied voltage at a particular frequency to study the following:

- Wire case 1A: Comparing the analytical calculation and simulation results.
- Wire case 1B: Vertical polyline: Potential of the wire is studied along a vertical line at the inlet (voltage applied surface) as shown in Figure 4.5.

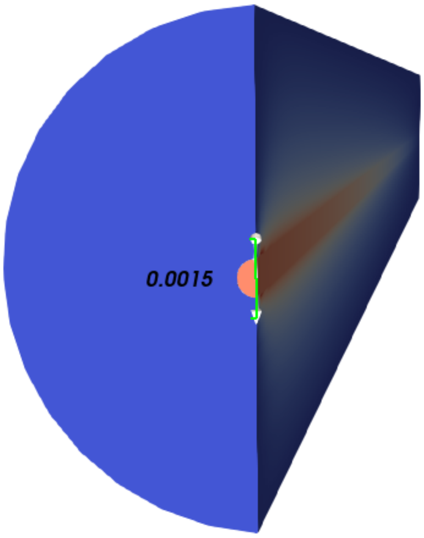

Figure 4.5: Vertical polyline setup at the inlet on the wire model (height depicted in SI units)

Wire case 2: A frequency domain simulation of the wire model to study the impedance behavior using bode plot.

Wire case 3: A frequency sweep measurement is taken using Bode 100 VNA to validate the impedance behavior from the simulation.

4.2.3.1 Wire case 1A: Comparing analytical calculation

Input data:

- Radius of the wire: $R = 3.75 \times 10^{-4}\,\mathrm{m}$
- Length of the wire: $L_w = 0.078\,\mathrm{m}$
- Electric conductivity of copper: $\sigma = 59.59 \times 10^{6}\,\mathrm{A/m \cdot V}$
- Resistivity of copper: $\rho = 1.678 \times 10^{-8}\,\Omega \cdot \mathrm{m}$
- Permeability of free space: $\mu_0 = 4\pi \times 10^{-7}\,\mathrm{T \cdot m/A}$
- Voltage applied: $V = 1\,\mathrm{V}$
- Frequency: $F = 100\,\mathrm{Hz}$

Calculation for the Current density:

- Resistance of the wire:

$$R = \frac{\rho \cdot L_w}{A} = \frac{1.678 \times 10^{-8} \cdot 0.078}{\pi \cdot (3.75 \times 10^{-4})^2} = 2.96 \times 10^{-3}\ \Omega \tag{4.1}$$

- Current through the wire:

$$I = \frac{V}{R} = \frac{1}{2.96 \times 10^{-3}} = 337.83\ \mathrm{A} \tag{4.2}$$

- Current density:

$$J = \frac{I}{A} = \frac{337.83}{\pi \cdot (3.75 \times 10^{-4})^2} = 7.64 \times 10^{8}\ \mathrm{A/m}^2 \tag{4.3}$$

Thus, the calculated current density is $7.64 \times 10^{8}\ \mathrm{A/m}^2$. Given that the calculations are performed at a relatively low frequency of 100 Hz, it is reasonable to assume that the inductive and capacitive effects in the wire are negligible. Therefore, the impedance is dominated by the DC resistance and can be approximated as $Z \approx R$. Accordingly, at 100 Hz, the impedance is calculated to be $Z = 2.96 \times 10^{-3}\ \Omega$.

Calculation for the cutoff frequency:

- Inductance of the wire:

$$L = \frac{\mu_0 \cdot L_w}{2\pi} \left(\ln \left(\frac{2 \cdot L_w}{r} \right) - 0.75 \right) \tag{4.4}$$

$$\begin{aligned} &= \frac{4\pi \times 10^{-7} \cdot 0.078}{2\pi} \left(\ln \left(\frac{2 \cdot 0.078}{3.75 \times 10^{-4}} \right) - 0.75 \right) \\ &= 82.37\,\mathrm{nH} \end{aligned}$$

- Cutoff frequency:

$$f_c = \frac{R}{2 \cdot \pi \cdot L} = \frac{2.96 \times 10^{-3}}{2 \cdot \pi \cdot 82.37 \times 10^{-9}} = 5722Hz \tag{4.5}$$

The cutoff frequency for the wire, based on the calculated resistance and inductance, is estimated to be 5722 Hz. This value will be referenced later in section 5.1.4, where the simulation results for wire case 2 are analyzed in detail.

Table 4.4: Comparing analytical calculation and simulation at 100 Hz for the wire case

	Impedance (mΩ)	**J - Current density (A/m^2)**
Analytical	2.96	7.64×10^8
Simulation	3.02	9.5×10^8

A comparison between the analytical calculations and simulation results for both impedance magnitude and current density is presented in Table 4.4. Both cases are evaluated at a frequency of 100 Hz. This comparison indicates that there is a close match between the simulation and analytical results, thus validating the solver outputs and the developed ElmerFEM script.

4.3 Coin Cell CR3032 model set-up

The scripts for solvers are tested using a sample coin cell battery test case before it is applied on the cylindrical cell model. For this purpose, a coin cell model is developed for this study based on an available CR3032 CAD model from internet resource [42]. The cross-sectional geometry of the developed coin cell model is presented in Figure 4.6, while the individual layers inside the coin cell are illustrated in Figure 4.7.

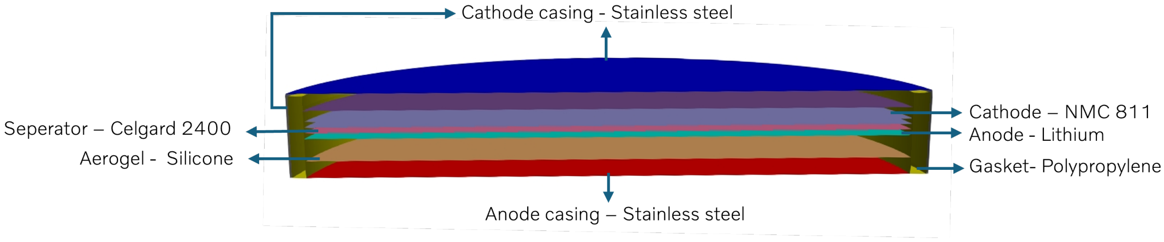

Figure 4.6: CR3032 Coin cell geometry cross-section

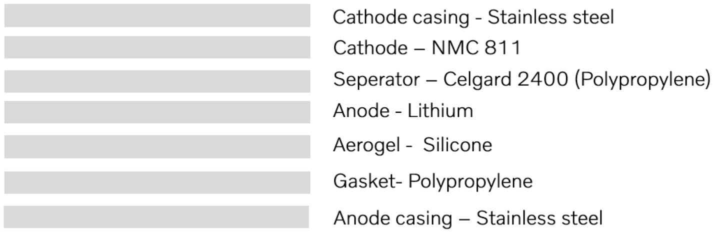

Figure 4.7: CR3032 Coin cell geometry layers

The material properties for the electrodes, casing, gasket and separator are obtained from COMSOL Multiphysics [43] and Materials Handbook [44]. The material properties used in the simulation are tabulated in Table 4.5.

Table 4.5: Material properties for coin cell: electrodes (Lithium, NMC), coin cell casing (Stainless Steel), separator (Polypropylene), and gasket (Silica) [43][44]

Property	**Lithium**	**NMC**	**Stainless Steel**
Density (kg/m^3)	5340	4870	7925
Sound Speed (m/s)	6000	4900	5100
Young's Modulus (Pa)	2.0×10^9	7.8×10^{10}	2.0×10^{11}
Poisson Ratio	0.340	0.25	0.285
Electric Conductivity (S/m)	1.07×10^7	1.0×10^2	1.824×10^6
Heat Capacity (J/kg·K)	3580	840.1	460
Heat Expansion Coefficient (1/K)	5.6×10^{-5}	1.2×10^{-5}	1.49×10^{-5}
Heat Conductivity (W/m·K)	84.8	10.3	24.0
Relative Permeability	0.999994	1	1.0003
Relative Permittivity	200	60	200

Property	**Polypropylene**	**Silica**
Density (kg/m^3)	905	2330
Sound Speed (m/s)	8433	8433
Young's Modulus (Pa)	1.85×10^{11}	1.85×10^{11}
Poisson Ratio	0.28	0.28
Electric Conductivity (S/m)	1.0×10^{-3}	1.0×10^{-3}
Heat Capacity (J/kg·K)	1700	555.8
Heat Expansion Coefficient (1/K)	4.68×10^{-6}	4.68×10^{-6}
Heat Conductivity (W/m·K)	427.3504	–
Relative Permeability	0.3	0.03
Relative Permittivity	2.25	3.8

4.3.1 Meshing

4.3.1.1 Surface mesh

The surface mesh was generated based on the configurations provided in Table 4.7. Ortho-tria is preferred element type due to it's accuracy and robust nature in handling irregular domains. Given the simple geometry of the coin cell model, the minimum mesh length for the surface mesh is set as low as 0.5 mm. The resulting surface mesh of the coin cell model is depicted in Figure 4.8. Since this model is used for testing the solver, mesh refinement is not considered.

Table 4.7: Surface mesh configurations for the Concept Model V2

S.No	Mesh parameter	Value
1	Element type	ortho tria
2	Element order	1st level
3	Growth rate	1.2
4	Distortion angle	15

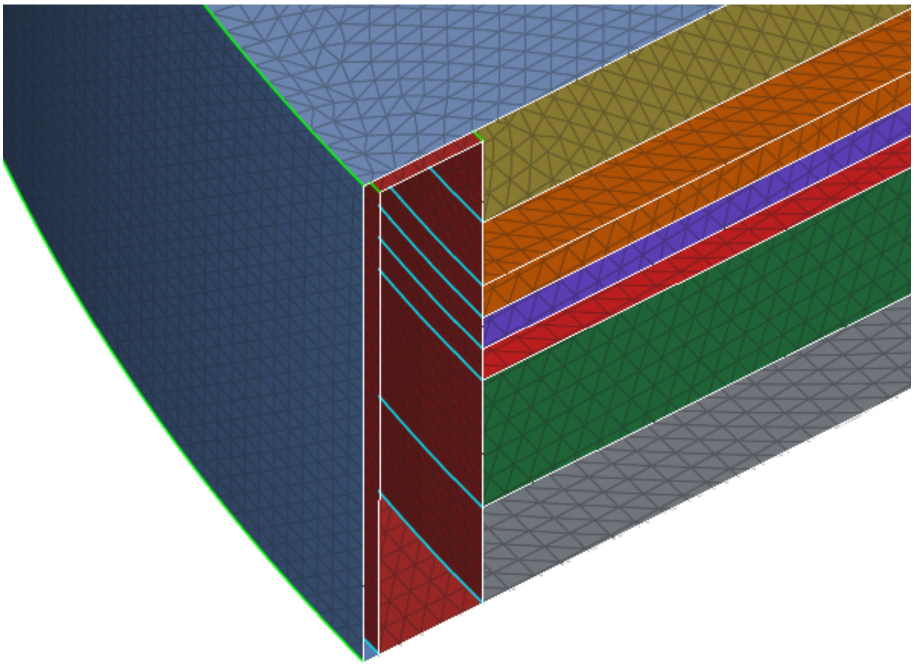

Figure 4.8: Surface mesh of the Coin cell model

4.3.1.2 Volume mesh

The volume mesh was generated using the default mesh configurations. The volume mesh of the coin cell model in ANSA as illustrated in Figure 4.9 consist of 6.3 Million mesh elements.

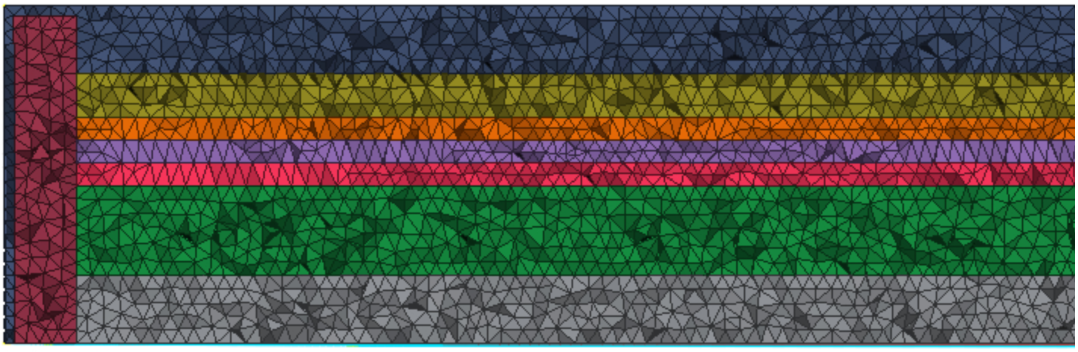

Figure 4.9: Volume mesh of the Coin cell model

4.3.2 Boundary Conditions

Cathode casing is the positive terminal at 3 V and the Anode casing is the negative terminal at 0 V as illustrated in Figure 4.10. The initial condition for temperature is set to 300 K. Body force is defined as joule heating in order to include heat generated while current flows through the cell, which is given as a heat source. Both inlet condition and body force are applied to all bodies in the coin cell.

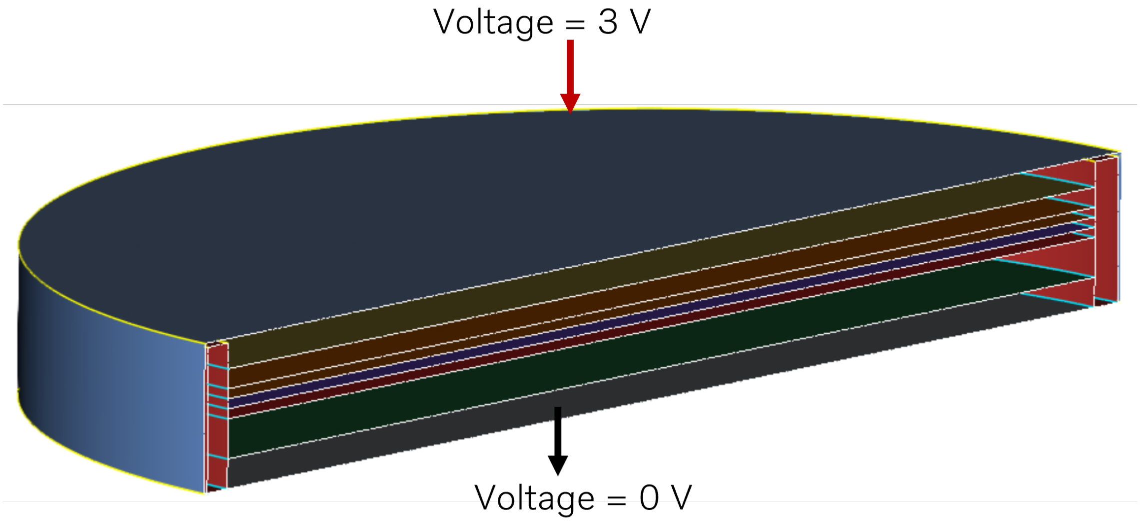

Figure 4.10: Coin cell electrical boundary conditions

4.3.3 Coin cell case study

Coin cell case 1: Vertical polyline: The potential distribution in the coin cell is studied along a vertical line as shown in Figure 4.11.

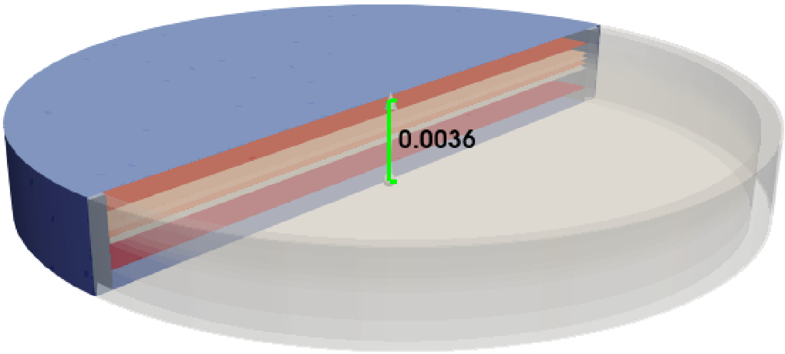

Figure 4.11: Vertical polyline setup for the coin cell model (height depicted in SI units)

Coin cell case 2: Impedance study: A frequency domain simulation of the coin cell model to study the impedance behavior using bode plot.

Coin cell case 3: Visualization: The potential distribution, electric field and magnetic flux vectors in the coin cell are studied to understand the solver outputs.

4.4 Cylindrical cell model set-up

4.4.1 3-D CAD model

A relatively detailed concept CAD model of a commercially available OEM large format cylindrical 46XX cell illustrated in Figure 4.12 was provided for this thesis.

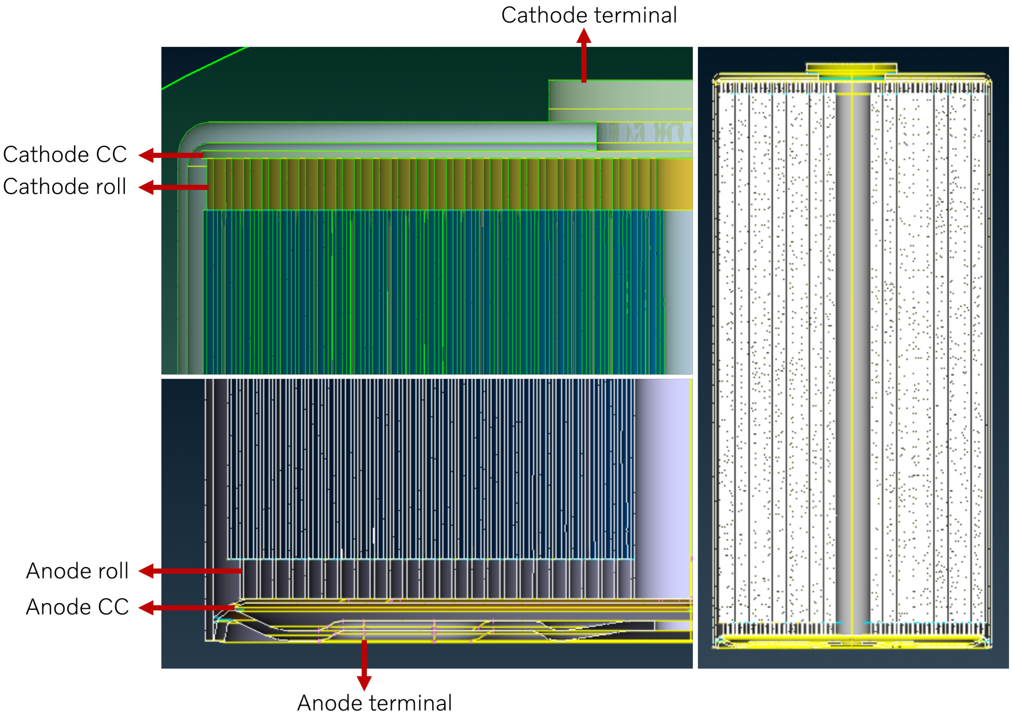

Figure 4.12: Original cylindrical cell Concept Model V1 *(*CC refers to the current collector)*

Table 4.8: Summary of discrepancies and modifications to the Concept Model V1

S.No	Discrepancies	Modifications
1	Concept Model V1 has tabless design for the electrode jelly roll.	Cathode jelly roll height is trimmed to same height as in the X-ray.
2	Cathode current collector is in contact with the cathode top plate.	Cathode current collector is moved to contact the cathode jelly roll.
3	Instersecting surfaces between electrodes and current collector.	Changes are made in the model to remove the intersections.
4	Double faces are identified on the electrode surfaces.	Removed double faces in the model.
5	Concept Model V1 is 46XX (46mm diameter and XXmm height) in dimension.	Model is scaled down from 46XX to 46XX dimension.

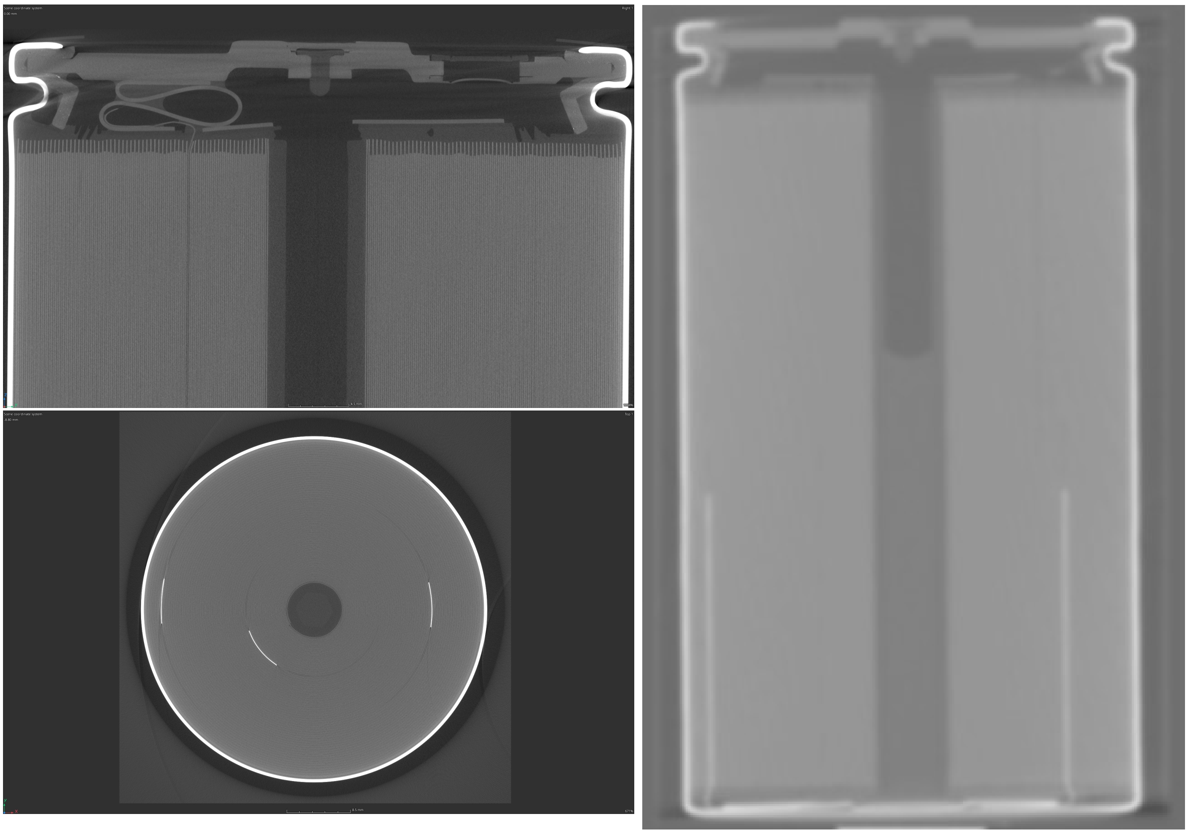

Figure 4.13: X-Ray images of the OEM cylindrical cell *(Image provided by Volvo Car Corporation Material Laboratory)*

The X-ray images of the selected OEM cell, as shown in Figure 4.13, reveal discrepancies between the physical cell and the available CAD model. Thus it is required to re-work on the CAD model to closely match the X-Ray images. The identified mismatches, along with the corresponding alterations implemented, are summarized in Table 4.8. These alterations are made using ANSA v25.1.0 software [28].

The identified discrepancies in the Concept Model V1, including intersecting surfaces and duplicate faces, could potentially lead to mesh irregularities. A revised CAD model, incorporating the modifications listed in Table 4.8, is developed. A far field is included in the model to understand the domain behavior around the cell under study. This updated Concept Model V2 is presented in Figure 4.14 and is utilized in the remainder of this study. While design modifications have been implemented, the resulting model more closely approximates the actual cell design; however, it does not fully represent the OEM 46XX cell.

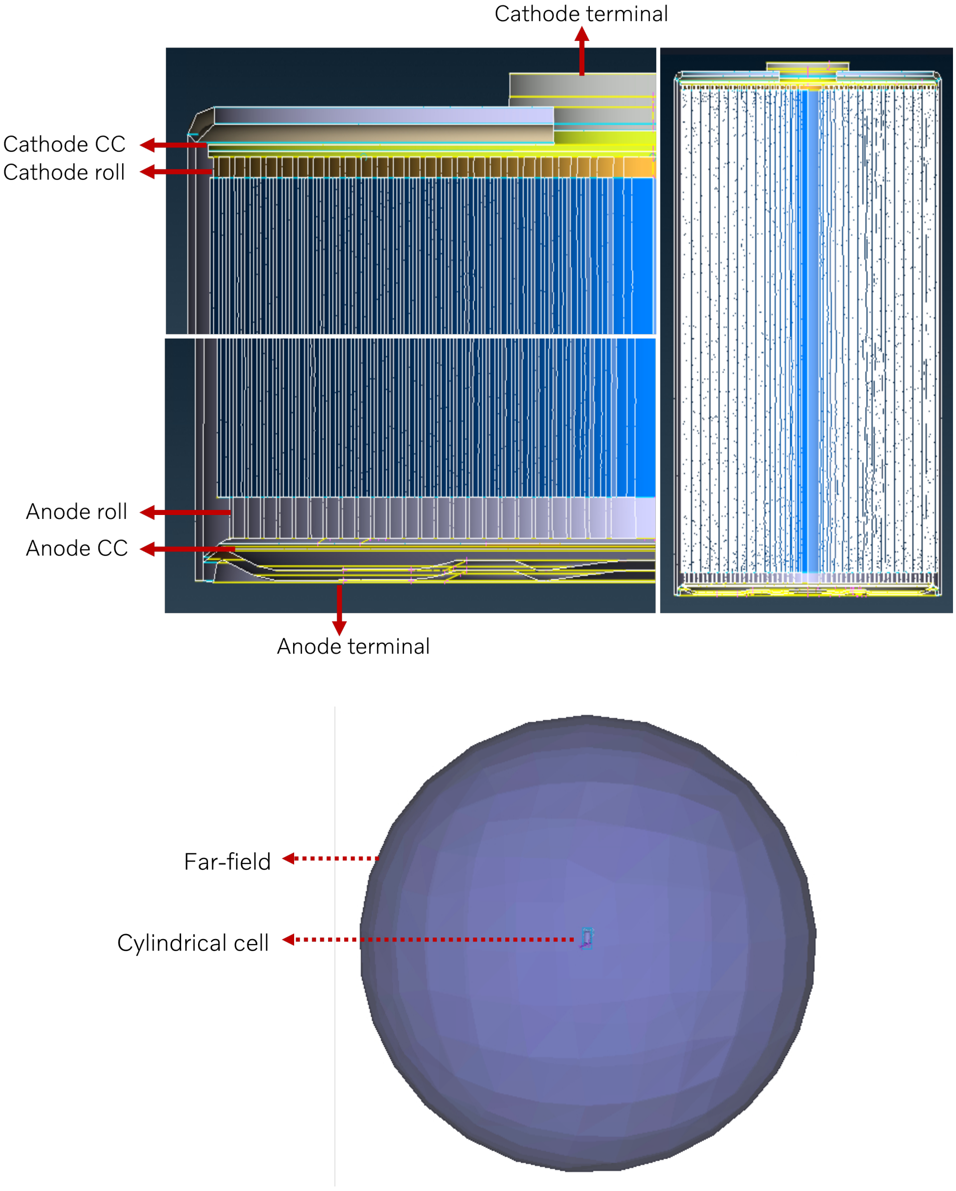

Figure 4.14: Concept Cell Model V2 (*CC refers to the current collector)

Far-field distance computation

For the purpose of far-field estimation, the battery cell is considered an Radio frequency (RF) source. The far-field boundary R_{far} is commonly calculated using the following equation [45]:

$$R_{\text{far}} \geq \frac{2D^2}{\lambda} \tag{4.6}$$

Where:

- D = largest characteristic dimension = 0.08 m
- λ = wavelength = $\frac{c}{f}$ [m]
- c = speed of the wave in vaccum = 3×10^8 m/s
- f = frequency [Hz]

The calculated R_{far} distance for the cylindrical cell Concept Model V2 is extremely small in nanometers because the RF source (battery cell) length is significantly smaller than the wavelength. Thus for electrically small RF source, the far-field region is defined using a rule of thumb, typically at a distance of approximately 3 wavelengths [46]. Therefore, in this study, the far-field is dimensioned based on the following simplified equation:

$$R_{\text{far}} = 3 \cdot \lambda \tag{4.7}$$

4.4.2 Material definition

The materials assigned to the cylindrical cell model are listed in Table 4.9. These materials are identified based on an internal tear-down analysis performed at Volvo Cars and verified with similar cylindrical cell studies found in the literature [47]. The properties for the defined materials are obtained from COMSOL Multiphysics [43], Materials Handbook [44] and other public resources available on the internet [48]. The material properties for the separator (polypropylene) and casing (stainless steel) are presented in Table 4.5, while the properties for cylindrical cell electrodes and current collectors are provided in Table 4.10.

Table 4.9: Cylindrical cell components and assigned materials

Components	**Material**
Jelly Cathode	LFP
Cathode current collector	Aluminium
Anode current collector	Copper
Jelly Anode	Graphite
Separator	Polypropylene
Casing	Stainless steel

Table 4.10: Material properties for cylindrical cell model: electrodes (LFP and graphite) and current collector (aluminium and copper)

Property	**Graphite**	**LFP**	**Aluminium**	**Copper**
Density (kg/m^3)	2300	3600	2700	8960
Sound Speed (m/s)	1470	5700	5000	3810
Young's Modulus (Pa)	1.15×10^{7}	1.178×10^{11}	7.0×10^{10}	1.15×10^{11}
Poisson Ratio	0.23	0.30	0.35	0.34
Electric Conductivity (S/m)	8.3×10^{4}	91	3.07×10^{7}	5.959×10^{7}
Heat Capacity (J/kg·K)	710	881	897	385
Heat Expansion (1/K)	0.6×10^{-6}	1.2×10^{-5}	23.1×10^{-6}	16.5×10^{-6}
Heat Conductivity (W/m·K)	10.3	1.0	237.0	401.0
Relative Permeability	1.0	1.0	1.0	0.999994
Relative Permittivity	10.0	4.5	1.0	1.0

4.4.3 Meshing

4.4.3.1 Surface mesh

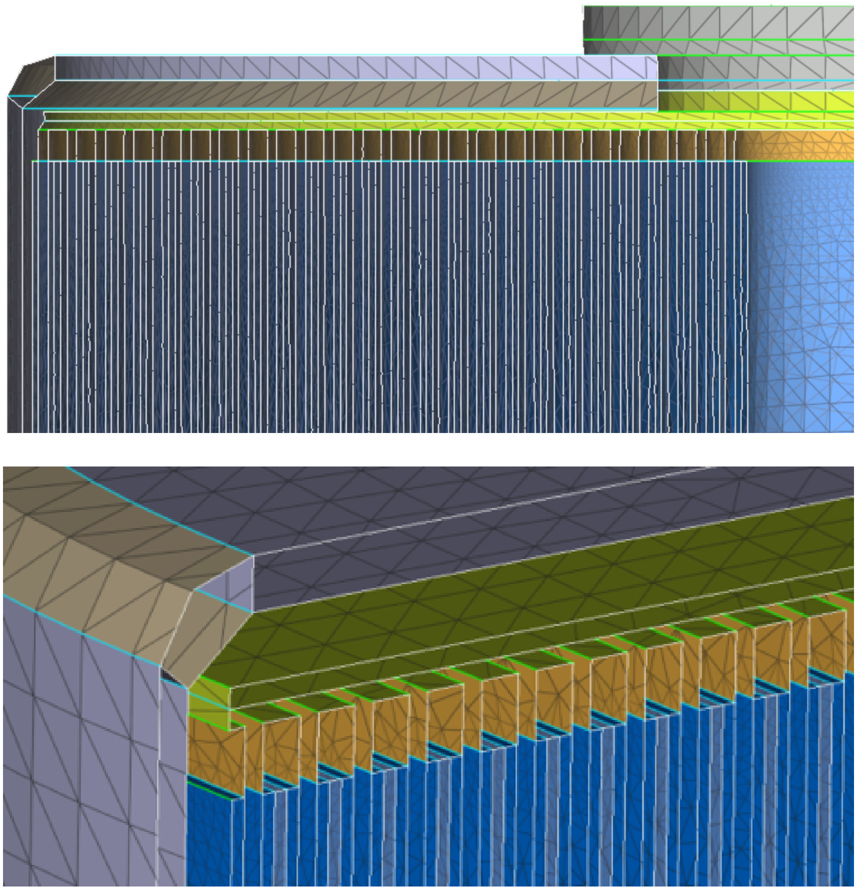

Figure 4.15: Surface mesh of the cylindrical cell Concept Model V2

Table 4.11: Surface mesh refinement for the Concept Model V2

Minimum mesh length	**Value [mm]**
Far field	5
Cell casing	1
Rest of the cell	0.08

The surface mesh is generated based on the mesh configurations as mentioned for the coin cell in Table 4.7. Mesh is refined as depicted in Figure 4.15 to improve the computational efficiency of the simulation model. It is refined for the mesh size in the far field, cell casing and the rest of the active parts in the cell as mentioned in Table 4.11.

4.4.3.2 Volume mesh

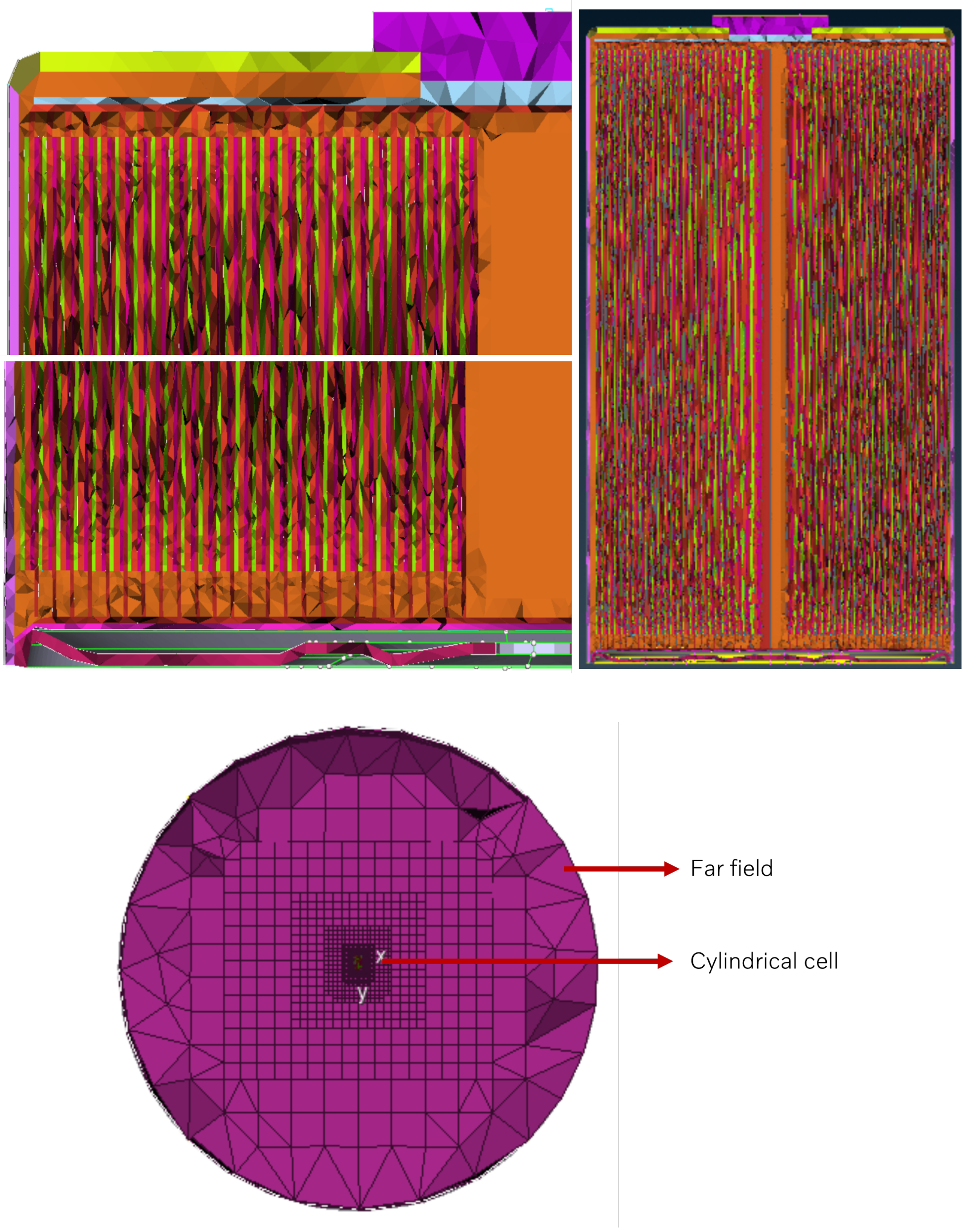

Figure 4.16: Volume mesh of the cylindrical cell Concept Model V2

As the volume mesh is derived from the generated surface mesh, its configuration is relatively straightforward. The hexapoly mesh element type is used due to its higher accuracy and better convergence tolerance, as discussed in Chapter 3. The volume mesh is generated by ANSA with a Maximum Aspect Ratio set to 4. This is aligned with Nastran mesh quality convention (used to eliminate warping, skew, double surfaces etc.). The Concept Model V2 in ANSA, illustrated in Figure 4.15 comprises 8.3 million mesh elements. A mesh level of 2 in the solver script increases the number of mesh elements to 16.6 million mesh elements.

4.4.4 Initial and boundary conditions

The cell is subjected to electrical, thermal and mechanical conditions. The electrical (voltage) conditions of the cell are as shown in Figure 4.17. The following initial and boundary conditions are applied for the cell simulation:

- The initial temperature condition is set to 300 K for all boundaries
- Voltage at the cathode terminal is set to 3.2 V.
- Voltage at the anode terminal is set to 0 V.
- Temperature at the casing wall is set to 300 K.
- Heat Transfer Coefficient (HTC) of 4 W/m^2K is applied only to casing wall.
- Displacement in the casing is set to 0 m in the Z-direction.

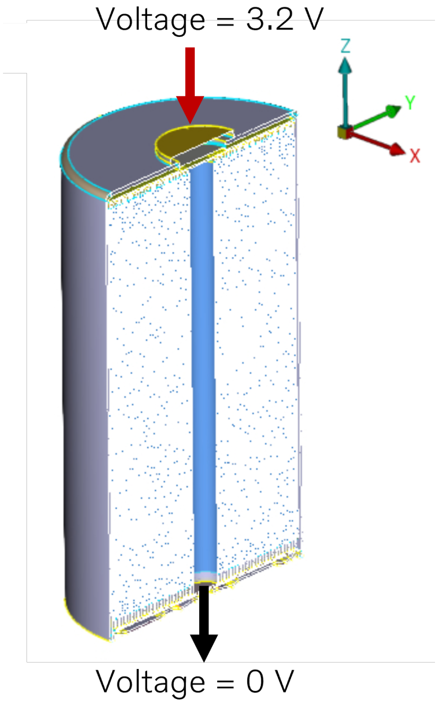

Figure 4.17: Cylindrical cell electrical boundary conditions

The temperature values are based on ambient room temperature. The applied voltage follows the representative cell datasheet and is verified on the physical cell using a calibrated Fluke digital multimeter [49]. The HTC is based on natural convection, as this represents worst-case scenario. As the cell is allowed to swell in the X-Y axis, the displacement in Z-direction in the casing is restricted.

The following body forces are applied on all the cylindrical cell bodies:

- The joule heating computed by the MagnetoDynamics solver.
- The nodal forces computed by the MagnetoDynamics solver are used as displacement loads.

4.5 Experimental set-up

The measurements for the wire and cylindrical cell are taken using the Vector Network Analyzer (VNA) - Bode100. The measurement data was logged using Bode Analyzer Suite 3.5.1 tool. Shunt-through impedance analysis method is used for measurement due to its sensitivity for low impedance values and recommended impedance range from 1 mΩ to 100 Ω. More information about the shunt-through method and the other impedance measurement methods are discussed in Chapter 3. The schematic of the setup using the shunt-through method is shown in Figure 4.18, which is taken from the OMICRON LAB webpage [34].

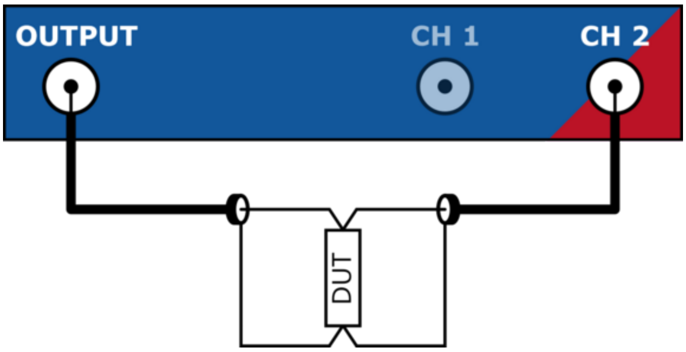

Figure 4.18: Shunt-through impedance analysis method schematic

4.5.1 Calibration

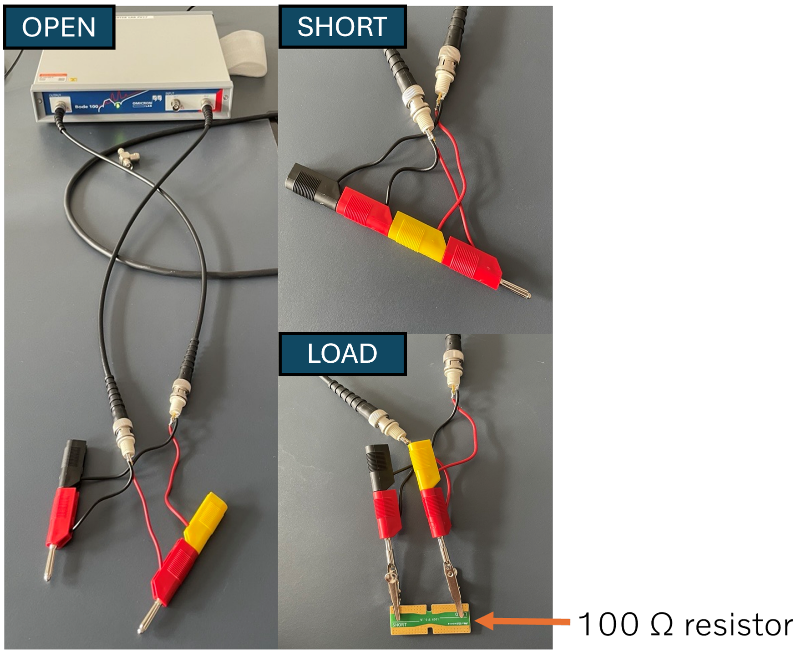

Figure 4.19: Experimental setup for calibration

The following three calibration techniques were used: open circuit, short circuit and load test. It's also known as the Open-Short-Match (OSM) calibration. The setup used for the calibration are as shown in figure 4.19.

The load test was performed using a 100 Ω resistor. The impedance value of 100Ω in the bode plot for the resistor load as in Figure 4.20, confirms the validity of the calibration.

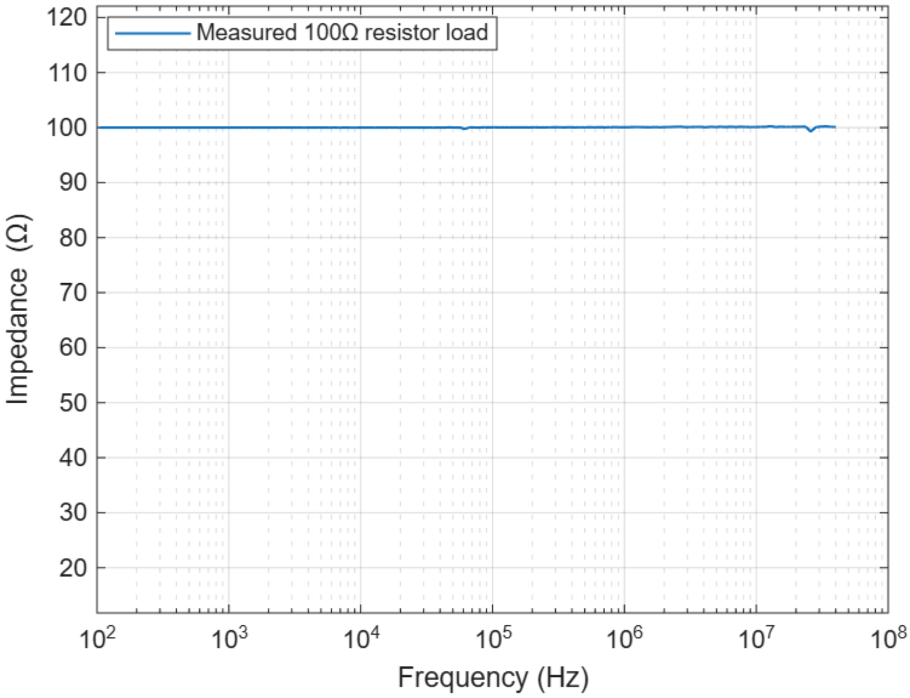

Figure 4.20: Measured impedance magnitude vs frequency for the 100Ω calibration load

4.5.2 Cylindrical cell measurement setup

In order to connect the cylindrical OEM cell to the Bode100 device, nickel strips are spot welded on the electrode terminals as in Figure 4.21. This is done to reduce the contact resistance at the cell terminals. Cables are soldered to the nickel plate and the female banana adapters are attached to the cables. An intermediate male banana adapter counterpart is used between the measuring equipment and the DUT. The overall connection setup between the OEM cell and the Bode100 device is as shown in Figure 4.22.

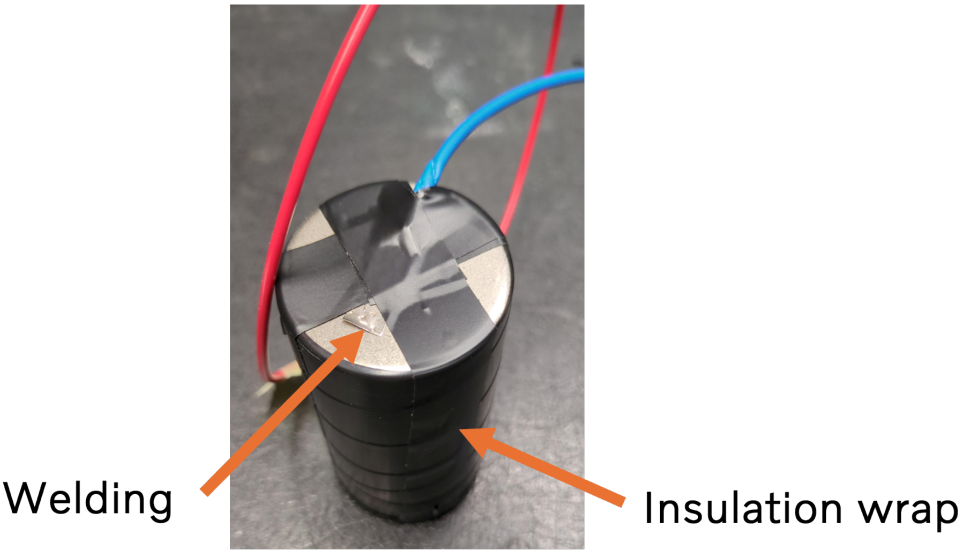

Figure 4.21: Cylindrical cell modified for experiment

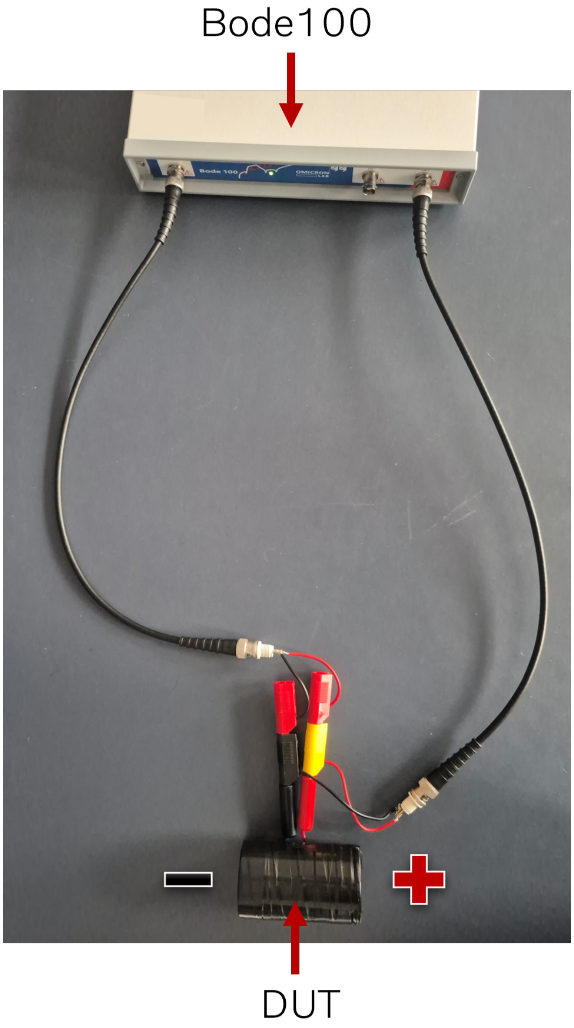

Figure 4.22: Cylindrical cell measurement setup

4.5.3 Bode Analyzer Suite configuration

The software interface and the implemented settings are shown in Figure 4.23. The data presented in this image correspond to the same plot used for the 100 Ω resistor load calibration, as shown in Figure 4.20. The configurations listed below were selected based on their reduced fluctuations and improved repeatability of the measured results:

- Frequency sweep is set from 1 Hz to 40 MHz. Since the machine limit is 100 MHz, the measurements are conducted at a lower threshold to avoid noise that may be introduced near the machine limit.
- The number of data points to be logged is set to 200.
- The source level is set to constant at 0 dBm.
- The attenuation at the receiver end is set to 20 dB. Note that only receiver 2 is connected during shunt-through method.
- Receiver bandwidth is set to 300 Hz.

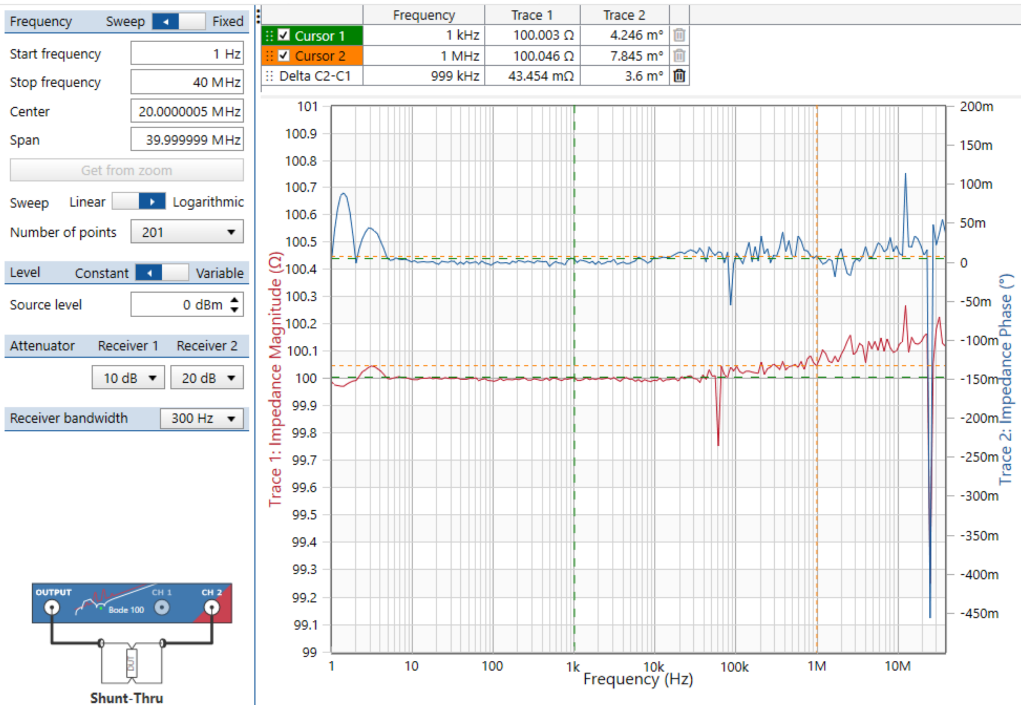

Frequency: Sweep / Fixed

Start frequency: 1 Hz

Stop frequency: 40 MHz

Center: 20.0000005 MHz

Span: 39.999999 MHz

Sweep: Linear / Logarithmic

Number of points: 201

Level: Constant / Variable

Source level: 0 dBm

Attenuator: Receiver 1: 10 dB; Receiver 2: 20 dB

Receiver bandwidth: 300 Hz

	Frequency	Trace 1	Trace 2
☑ Cursor 1	1 kHz	100.003 Ω	4.246 m°
☑ Cursor 2	1 MHz	100.046 Ω	7.845 m°
Delta C2-C1	999 kHz	43.454 mΩ	3.6 m°

Figure 4.23: Interface and configurations in Bode Analyzer Suite

4.6 Model tuning using genetic algorithm

An automated approach to optimize the cell parameters helps in tuning the cell for improved performance at high frequencies. A framework for multi-objective balancing of the cell parameters is developed using genetic algorithm (GA) as shown in Figure 4.24. Dakota version 6.10 software [38] is used to run genetic algorithms for the model and post-processing of the Dakota results is performed using Gnuplot, a command-line driven tool for graph generation [39].

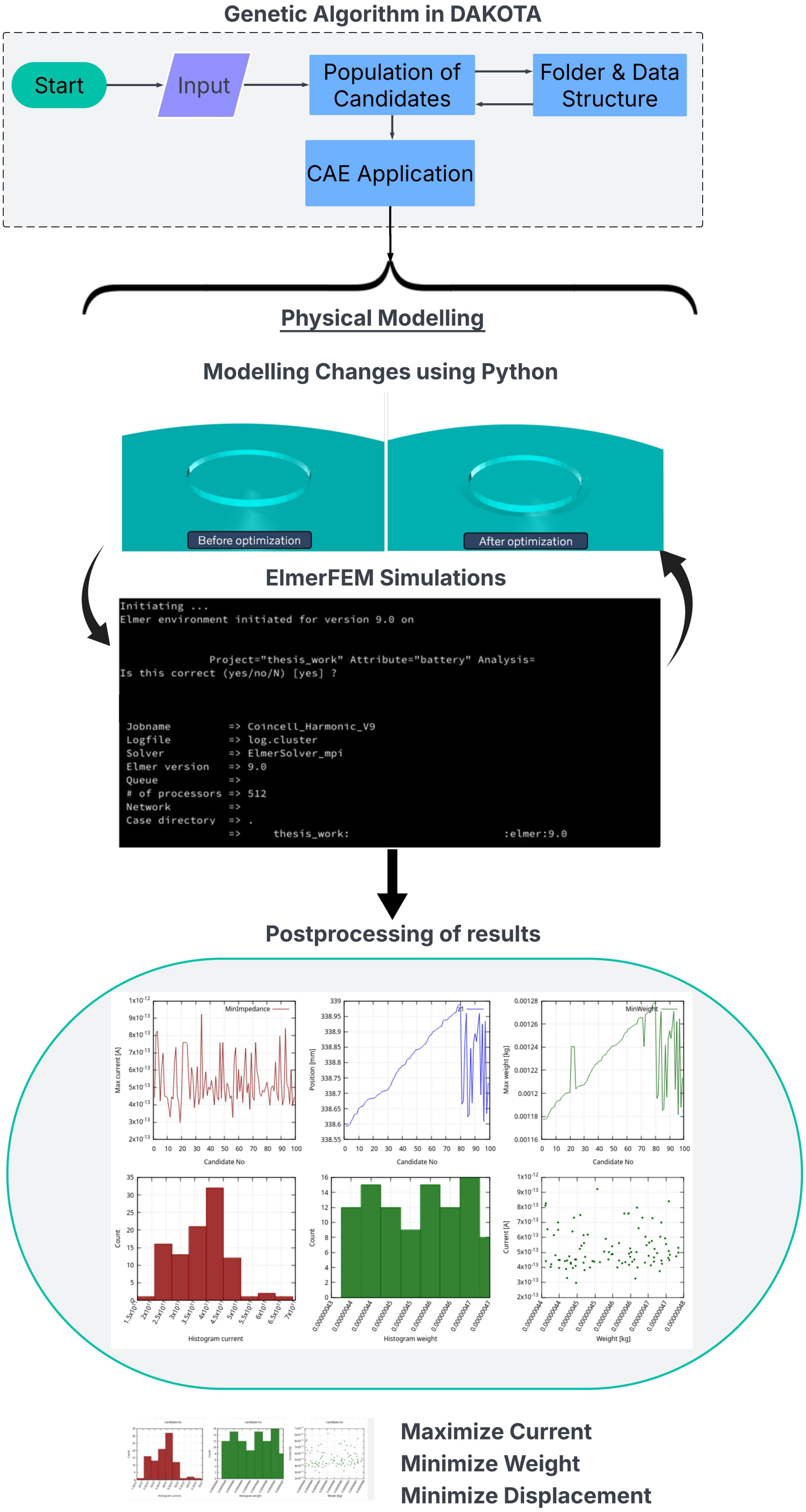

```
Initiating ...
Elmer environment initiated for version 9.0 on


              Project="thesis_work" Attribute="battery" Analysis=
Is this correct (yes/no/N) [yes] ?



 Jobname         => Coincell_Harmonic_V9
 Logfile         => log.cluster
 Solver          => ElmerSolver_mpi
 Elmer version   => 9.0
 Queue           =>
 # of processors => 512
 Network         =>
 Case directory  => .
                 =>     thesis_work:                     :elmer:9.0
```

Figure 4.24: Workflow for balancing multiphysics objectives using GA

A Multi-Objective Genetic Algorithm (MOGA) is preferred over Single-Objective Genetic Algorithm (SOGA) as it allows computing a set of trade-off solutions that can be optimized for multiple objectives simultaneously. Unlike a weighted-sum method, MOGA treats each objective function independently. Therefore it searches for solutions that are non-dominated, which indicates no other solution is better in all objectives.

4.6.1 Case set-up for automation pipeline

In a demonstrative example for testing the framework, the current collector topology is modified using GA. For this case, the multi-objective function is set to maximize the current, minimize weight and minimize displacement of the current collector. Maximizing the current flow correspond to reducing the impedance.

The overview of the automation process in Dakota is as follows:
- The mesh point ID's in the current collector, as shown in Figure 4.25, are repositioned within the set geometric limits (upper and lower bounds) defined in the python script, thereby generating a new candidate in each iteration of the GA.
- Using the new geometry, a mesh file is generated for each candidate followed by the mesh partitions for parallelization.
- Following that the pipeline runs an ElmerFEM simulation on the cluster for every candidate to meet the defined goals.
- The field results for the objective parameters are stored for post-processing before the mesh ID's are again modified to generate the new candidate.

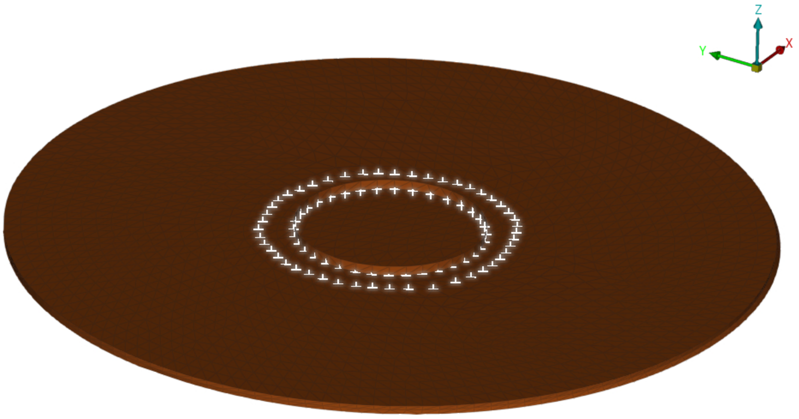

Figure 4.25: Mesh ID's for the current collector topology

The developed computational pipeline runs large-scale simulations where the GA continuously adapts the geometric parameters to meet the defined multi-objective balancing goals. This approach enables automated data-driven optimization of the battery cell design for multiple parameters and varying operating conditions. This allows to develop a scalable design environment to ensure enhanced performance and reliability, as well as an ability to scale the set up for larger systems.

4.6.1.1 Genetic algorithm model parameters

The configured model parameters for MOGA are presented in Table 4.12. In this section, the reasoning underlying the most important model parameter values is presented.

Table 4.12: MOGA control parameters used in Dakota

Parameter	**Value**
Population size	80
Maximum function evaluations	300
Initialization type	unique_random
Crossover type	shuffle_random
Number of offspring	40
Number of parents	20
Crossover rate	0.8
Mutation type	replace_uniform
Mutation rate	0.05
Fitness type	domination_count
Replacement type	below_limit = 6
Shrinkage percentage	0.9
Niching type	distance (0.05, 0.05, 0.05)
Postprocessor type	orthogonal_distance (0.05, 0.05, 0.05)
Convergence type	metric_tracker
Percent change (convergence)	0.001
Number of generations	40

Population size sets the number of candidate solutions to 80. This is a moderate number allowing diversity while maintaining a reasonable computational time. The upper limit on the number of times the objective functions are evaluated is set to 300, directly affecting the solution and the total computational time. To improve initial diversity of the solutions, initialization type is given as unique random. Therefore, MOGA is initialized with randomly generated unique candidates in the beginning.

The relatively high crossover rate of 0.8 increases the probability of recombination between selected parents and favors combining good solutions. The probability of mutating each gene is set to 5%. This value maintains exploration without disrupting good solutions. Fitness type is set to dominant which drives the pareto front to approach based on dominance ranking (how many solutions dominate a candidate). The distance of 0.05 for the niching and post-processing ensures reasonable spread along the Pareto front without allowing the solutions to form a cluster.

Chapter 5

Analysis

5.1 Harmonic wire model

5.1.1 Wire case 1B: Vertical polyline

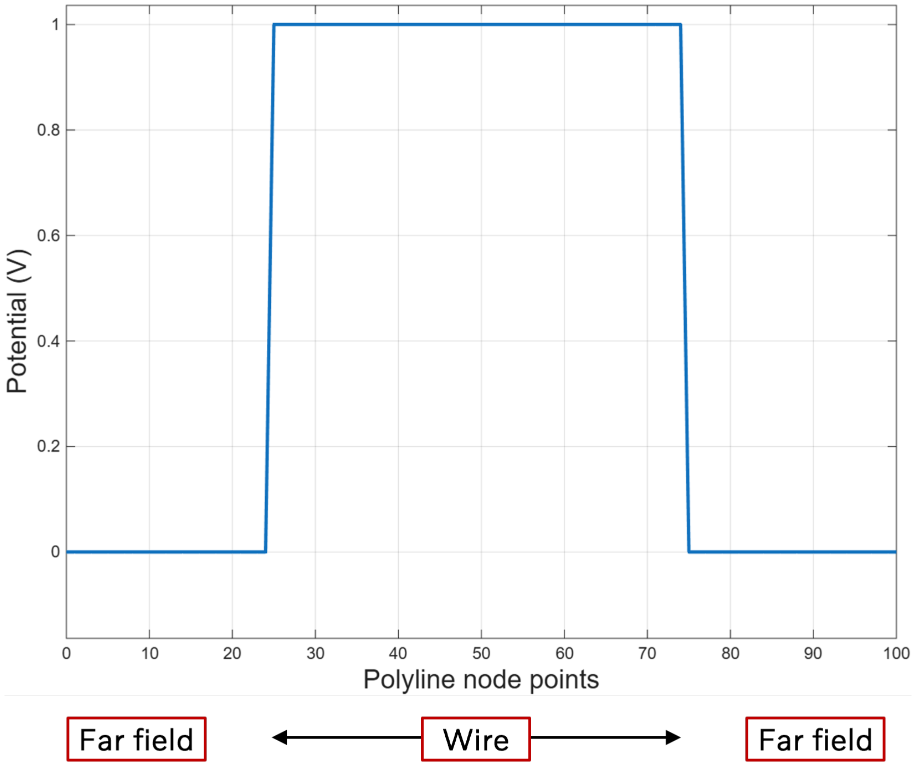

Figure 5.1: Potential distribution along a vertical polyline

The simulation setup for the vertical polyline at the inlet is presented in Figure 4.5. Due to the presence of the wire, the potential magnitude along the polyline is expected to increase and reach 1 V in the mid-region of the polyline node points. This is verified as shown in Figure 5.1. The potential drops to 0 V as the polyline points move away from the wire region. It is inferred from the results in wire case 1B that, the potential of the wire behaves as expected and the ElmerFEM solver output is verified.

5.1.2 Wire case 2: Impedance plot

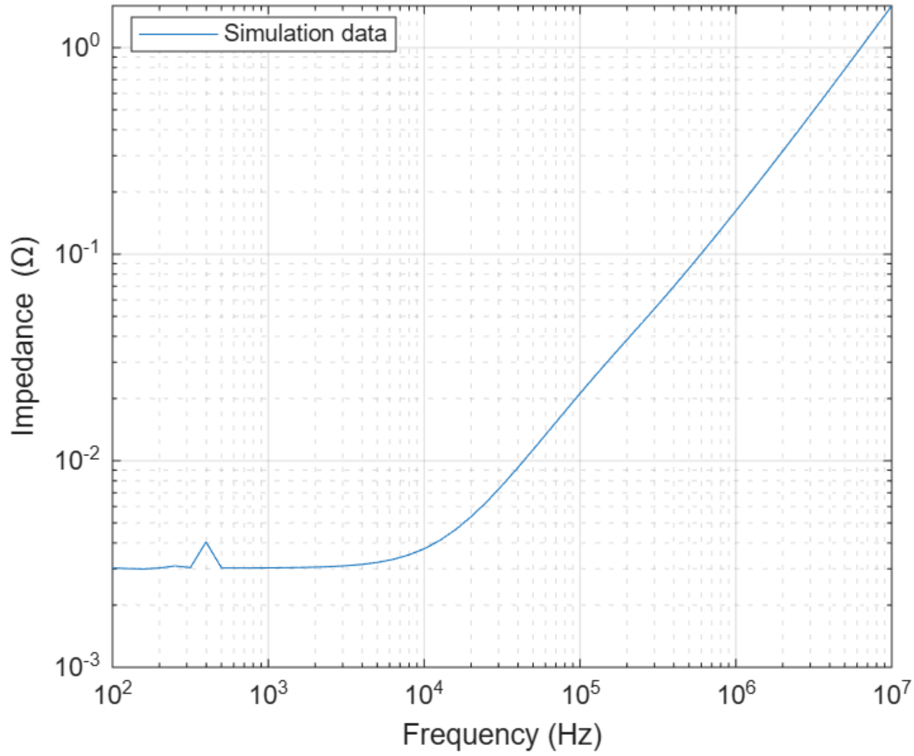

(a)

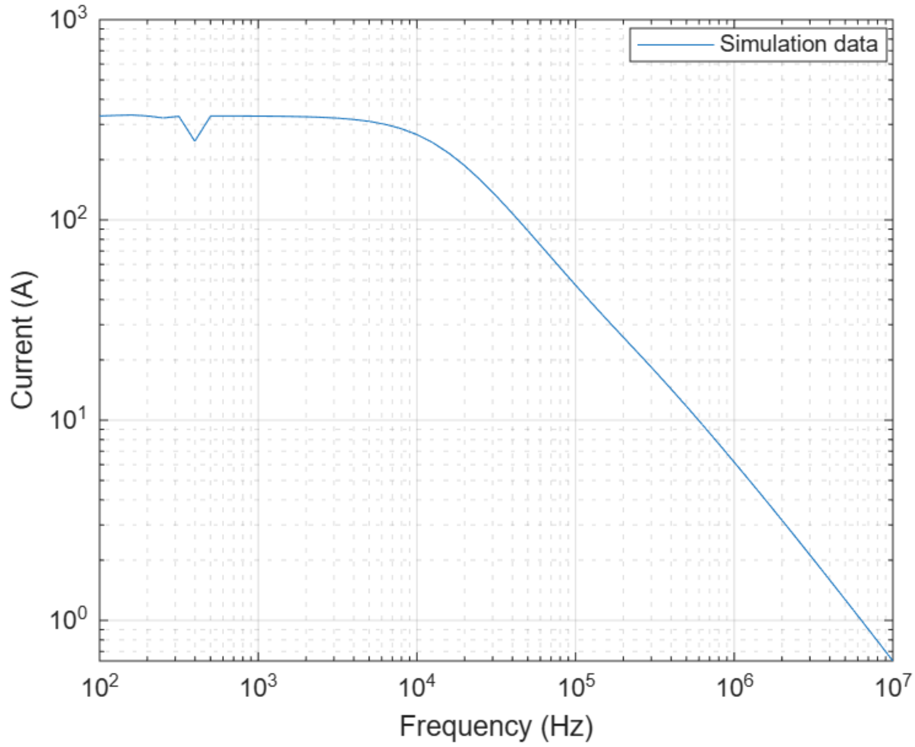

(b)

Figure 5.2: (a) Simulated impedance magnitude vs frequency for the wire model (b) Induced current plot for the wire model

The bode plot for the wire model is illustrated in Figure 5.2, where the impedance increases over the frequency spectrum. At the mid-frequency region starting from 100 Hz, the resistive component is predominant in the wire leading to a constant impedance value. While at high frequencies, the wire exhibits dominant inductive behavior causing a rise in impedance. This inductive effect is mainly due to length of the wire and the changing magnetic field around the wire. It is also noticeable from the current plot that impedance is inversely related to the induced current.

5.1.3 Wire case 3: Experimental results

The measurements are performed wtih Bode 100 VNA using the Impedance Adapter method, employing a B-WIC setup. The experimental bode plot results illustrated in figure 5.3 exhibits the expected inductive behavior at high frequencies.

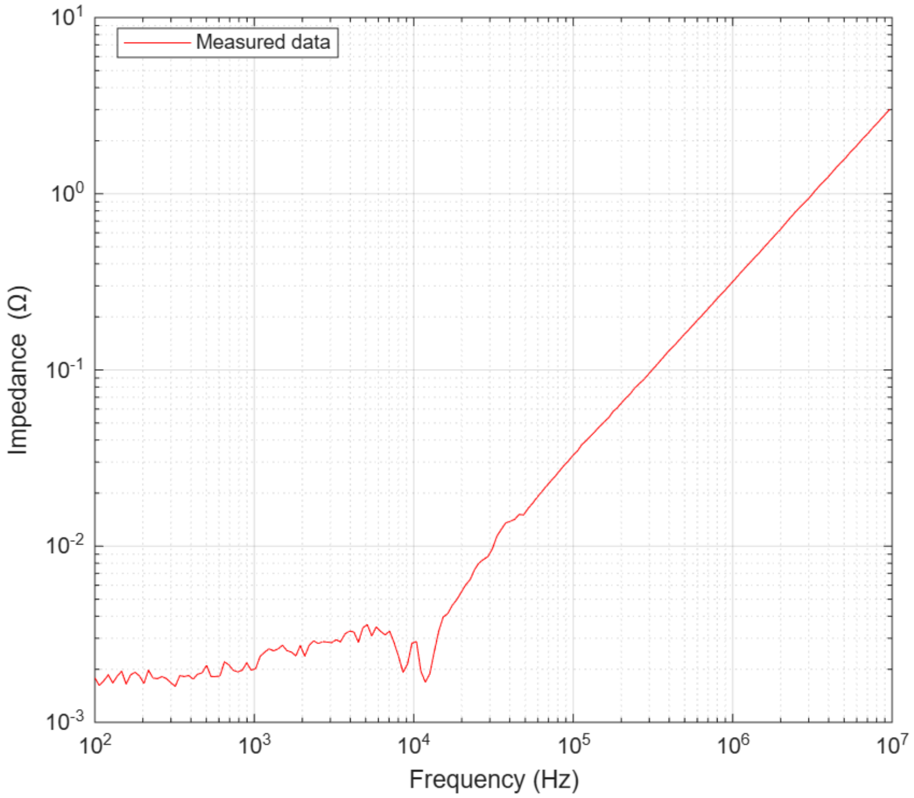

Figure 5.3: Measured impedance magnitude vs frequency for the wire model

5.1.4 Simulation model validation

The trend is found to be similar between the experimental and simulation results for the wire model as seen in Figure 5.4. A deviation in the magnitude is observed at low frequencies and very high frequency regions. This is noticeable deviation could be due to the following reasons:

- Measurements are conducted on a multi-stranded copper cable while the simulation is performed for a solid cylindrical block of copper cable.

- Simulation deploys pure copper for the material, whereas in reality, the copper strands are doped with elements like phosphorus and tin, and are insulated with an enamel coating.

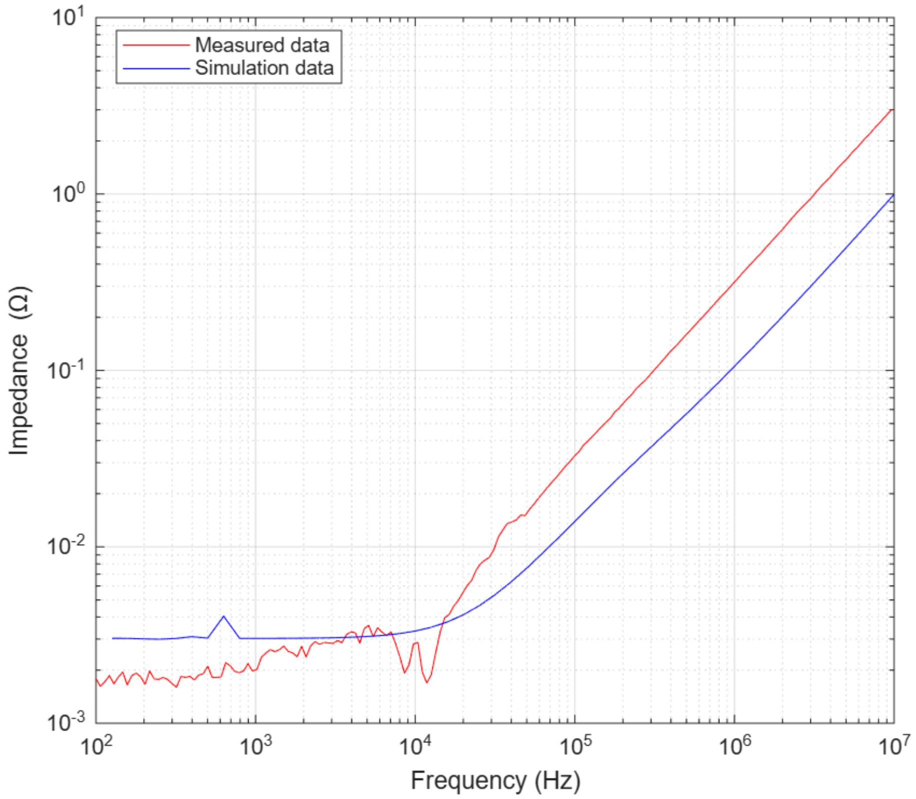

Figure 5.4: Simulation and experiment comparison; Impedance magnitude vs frequency for the wire model

Table 5.1: Comparing analytical, simulation and measurement for the wire model

	Impedance at 100 Hz (mΩ)	**Impedance at 5 kHz** (mΩ)	**Cutoff frequency (kHz)**
Analytical	2.96	-	5.72
Simulation	3.02	3.22	5.01
Measurement	1.79	3.58	8.5

Table 5.1 presents a comparison of impedance values and cutoff frequencies from analytical calculations, simulations, and experimental measurements. The analytical values are derived in the previous chapter and referenced from Table 4.4. This result indicates a reasonable correlation between analytical and simulation data. The comparison between simulated and measured impedance at 100 Hz reveals an offset of 68%, whereas at 5 kHz, the offset between these two cases decreases to around -11%. Although the impedance and cutoff frequency obtained from the measurements deviate slightly, they are within a comparable range in the high frequency region.

5.2 Coin cell CR3032

The second stage of this study involves analyzing a simplified battery cell using the validated solver setup. A coin cell was selected for this purpose due to its lower computational demand and ease of debugging.

5.2.1 Impedance study at various frequencies

5.2.1.1 Coin cell case 1: Vertical polyline

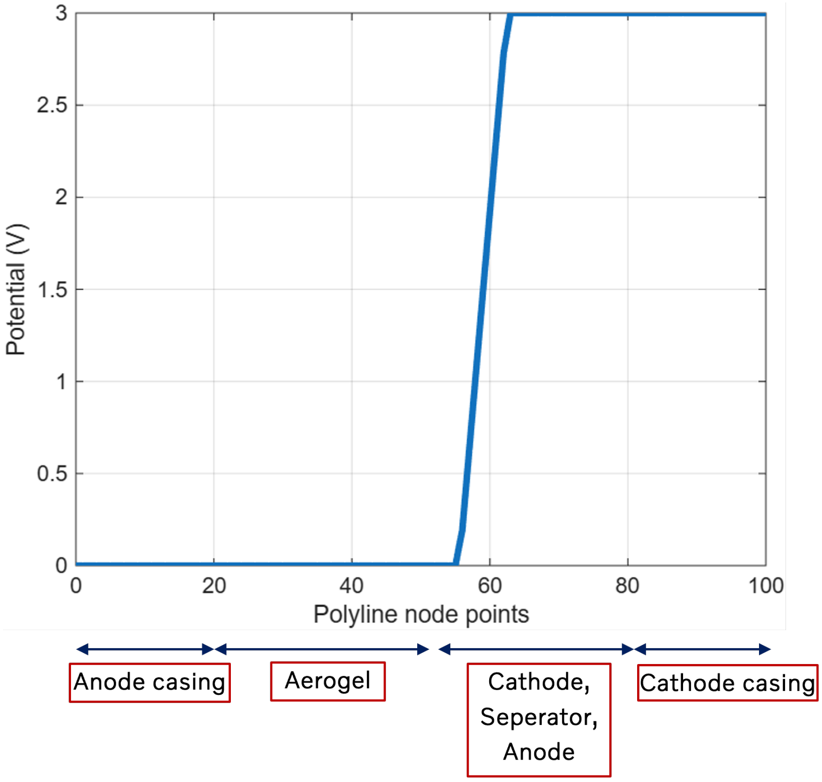

Figure 5.5: Potential variation along a vertical polyline along the mid-section of the coin cell model

The setup for the vertical polyline in the coin cell is presented in Figure 4.11. The results shown in Figure 5.5 indicate that a potential of 3 V is observed in the cathode casing and cathode regions. While the potential decreases from 3 V to 0 V across the separator and anode, remaining at 0 V (ground) throughout the aerogel and anode casing. Therefore, the potential across the terminals behaves as expected.

5.2.1.2 Coin cell case 2: Impedance study

The impedance behavior of the coin cell over the frequency is illustrated in Figure 5.6. The noticeable fluctuations in the impedance could be due to mesh detailing.

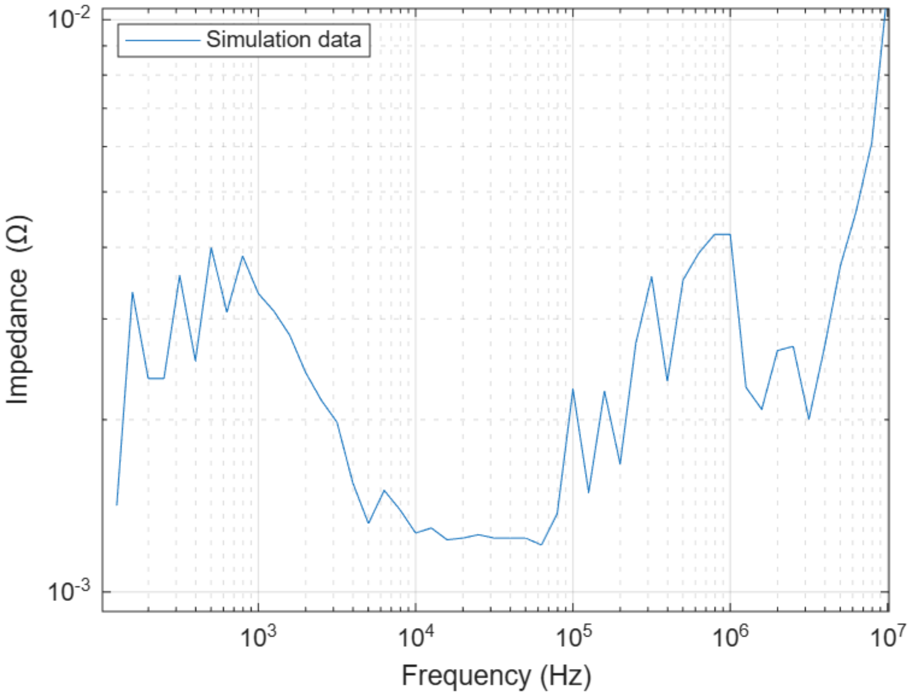

Figure 5.6: Simulated impedance magnitude vs frequency for the coin cell model

The initial drop in impedance in the high frequency region is attributed to the dominant capacitive effects. This is followed by a rise in impedance due to inductive behavior, which is an expected response from a simple coin cell battery.

5.2.1.3 Coin cell case 3: visualization

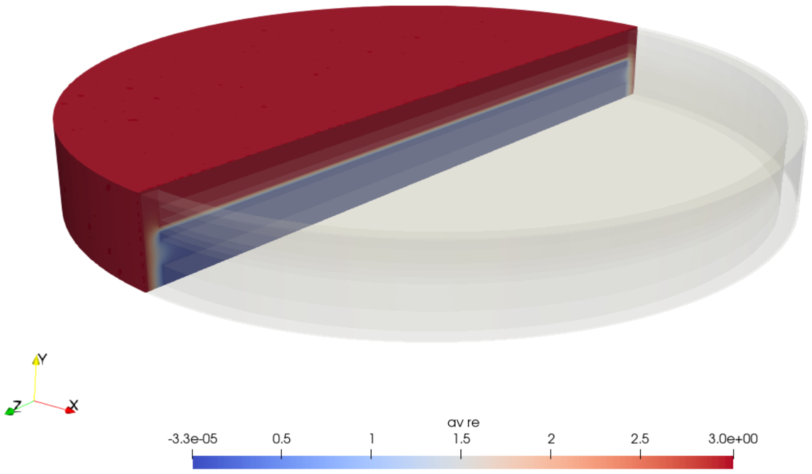

Figure 5.7: 3-D visualization of potential distribution at 5 kHz for the coin cell model

The 3D visualization of the potential distribution in Figure 5.7 indicates the highest potential of 3 V in the cathode region and a drop in voltage in the other regions of the coin cell. This visualization is aligned with the vertical polyline plot for potential as discussed earlier in section 5.2.1.1.

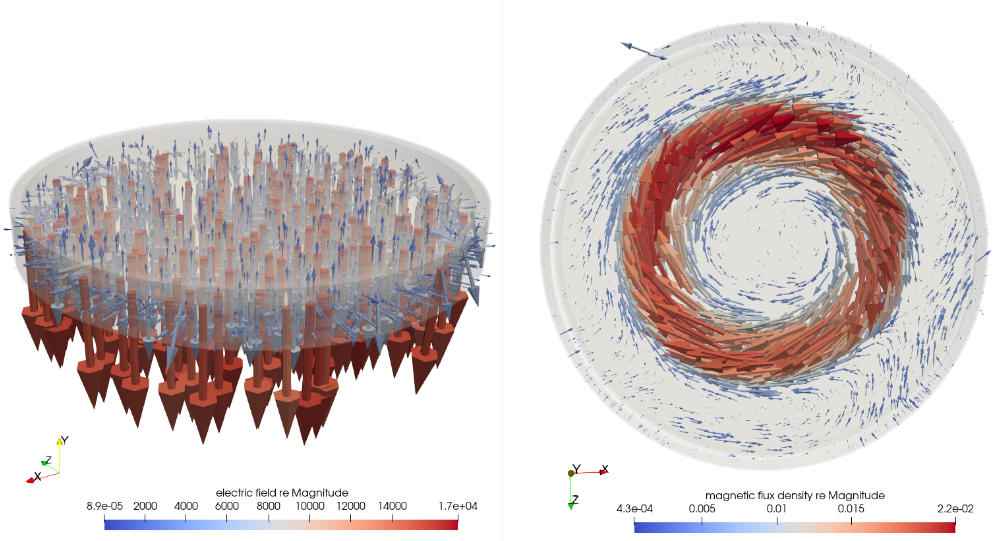

Figure 5.8: 3-D visualization of electric field and magnetic field vectors at 5 kHz for the coin cell model

The electric potential and electric field is related by the equation: $\mathbf{E} = -\nabla V$. This indicates that the electric field vectors are expected to point in the direction of decreasing potential. The electric field vectors for the coin cell model in Figure 5.8 behave as expected and act in the direction of potential drop. The direction of the magnetic field vectors is determined according to Maxwell's right-hand rule. According to Maxwell's right-hand rule (also known as the right-hand thumb rule), the flux path is expected to flow in a plane perpendicular to the direction of the current. Figure 5.8 shows that, from a top view, the magnetic field vectors follow a circular path when the current flows from cathode to anode.

The results from all three case studies in the coin cell validate the solver outputs, indicating that the model is suitable for applying to the cylindrical cells.

5.3 Cylindrical cell

The main scope of this thesis is to study the high frequency behavior of a cylindrical cell. Thus, the simulations are conducted for the mid-frequency and high frequency regions starting from 100 Hz up to 100 MHz. The test object in this case is a cylindrical OEM 46XX cell as discussed in the previous chapter.

5.3.1 Impedance study at various frequencies

The simulated impedance behavior of the cylindrical cell is illustrated in Figure 5.4. It is important to note that the moving average data filter is applied to the raw impedance data obtained from the simulation. This data filter takes the average of adjacent data points in the plot, thereby reducing sharp fluctuations or anomalies and producing a smoother graphical representation.

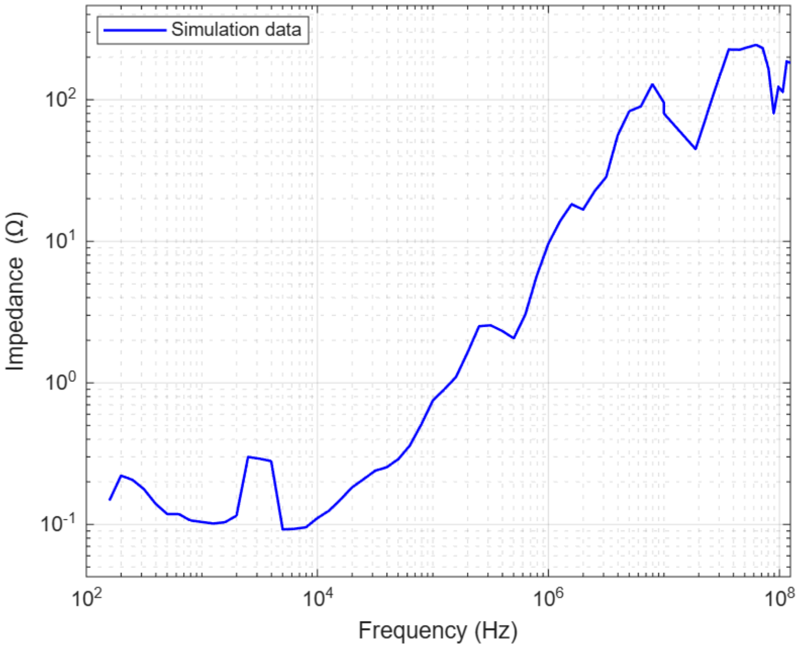

Figure 5.9: Simulated impedance magnitude vs frequency for the Cylindrical cell

It is noticeable that the mid-frequency region between 100 Hz and 1 kHz shows a declining trend in the impedance magnitude for the cylindrical 46XX cell, as expected from the referenced literature (Figure 3.7). The ion transfer is still relevant in this region but is low in dominance due to the transition from electrochemical to physical effects that affect the impedance of the cell.

Despite using the data filter, fluctuations are noticeable in the bode plot in in Figure 5.4 which might be due to irregularities during mesh generation or the tolerances set during the solver configuration.

5.3.1.1 High frequency behaviour

For the cylindrical cell under study, the high frequency region starts with the cut-off frequency. Beyond approximately the 8 kHz region, the impedance begins to increase. This rise in impedance is attributed to inductive effects from cell components such as the tabs and current collectors. These contribute to the parasitic inductance within the cell [6]. At high frequency, the electrochemical mechanisms such as ion transfer, double-layer formation and charge transfer reactions are too slow to respond and therefore becomes ineffective.

5.3.1.2 Experimental results

The measurements taken using Bode 100 follow similar trends to the bode plot results from the simulation discussed in the previous section. The measurement results have low fluctuations from the overall trend. This indicate that the modifications made on the cell to weld a nickel plate as mentioned in chapter 4 has resulted in improved contact resistance.

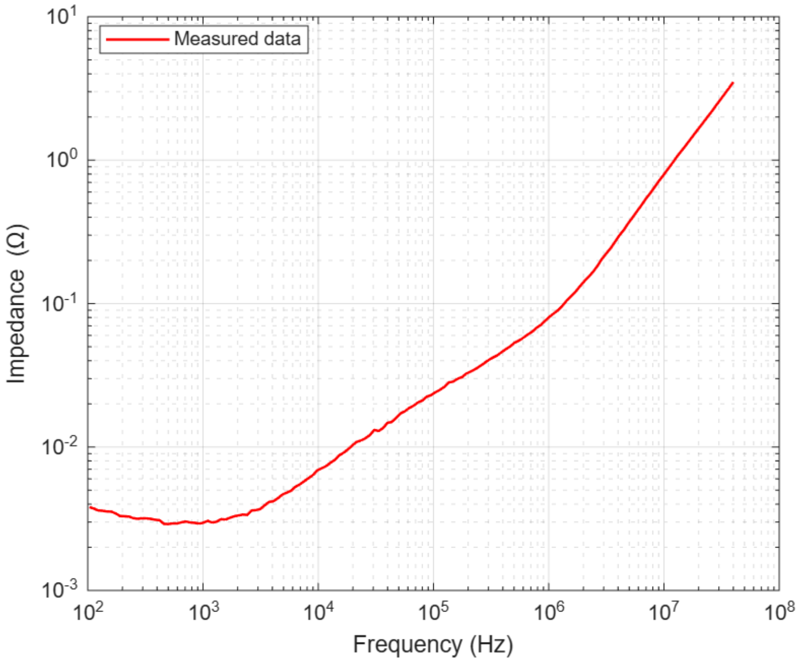

Figure 5.10: Measured impedance magnitude vs frequency for the Cylindrical cell

5.3.2 Visualization

The electromagnetic, thermal and structural behavior of the cylindrical cell are visualized using the ParaView tool.

5.3.2.1 Electromagnetic parameters

Figure 5.11 illustrates the distributions of electric potential, current density and magnetic flux density along the mid-section of the cylindrical 46XX cell at a frequency of 5 kHz. As expected, the potential is the highest at the cathode terminal at 3.2 V and lowest near the anode surface at 0 V. The visualization clearly represents the potential distribution between the terminals occurs through the current collectors, and subsequently through the electrode jelly rolls.

It is evident from the visualization that the current density is the highest at the current collectors. This is attributed to the accumulation of current from both the terminals and electrode jelly roll to the current collector. In comparison to the cathode top plate, which is directly connected to the cathode terminal, the casing wall exhibits a lower current density. While magnetic flux density becomes increasingly significant at lower frequencies, at 5 kHz it is observed to be higher in the cathode terminal and the electrode regions.

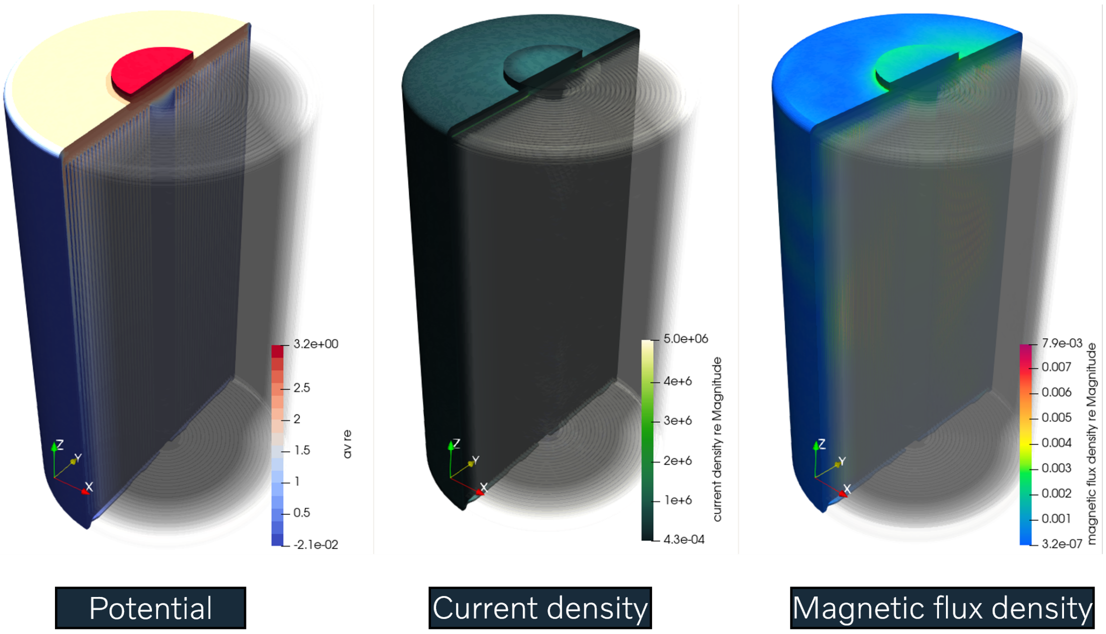

Potential

Current density

Magnetic flux density

Figure 5.11: 3-D visualization of electromagnetic parameters at 5 kHz

Magnetic flux density streamlines

The streamlines of the magnetic flux density inside the cell acts as an additional means of validating the solver outputs. As illustrated in Figure 5.12, seen from the top of the cell, the streamlines flow in a circular path as the current flows from the cathode to anode terminal. Therefore, the simulated flux streamlines are consistent with the expected behavior as described by Maxwell's right-hand rule.

Figure 5.12 also presents the magnetic flux streamlines at frequencies of 5 kHz and 1 MHz. It is observed that both the magnitude and the amount of flux streamlines significantly reduced at 1 MHz compared to 5 kHz. This decline can be due to rapid changes at high frequencies and skin effect, which creates resistance through magnetic field opposition, preventing the magnetic field from reaching higher magnitudes. While at lower frequencies, the magnetic field generated by the current has more time period to build up and reach higher magnitudes. Thus, the magnetic flux streamlines are more pronounced and consistent at 5 kHz than at 1 MHz.

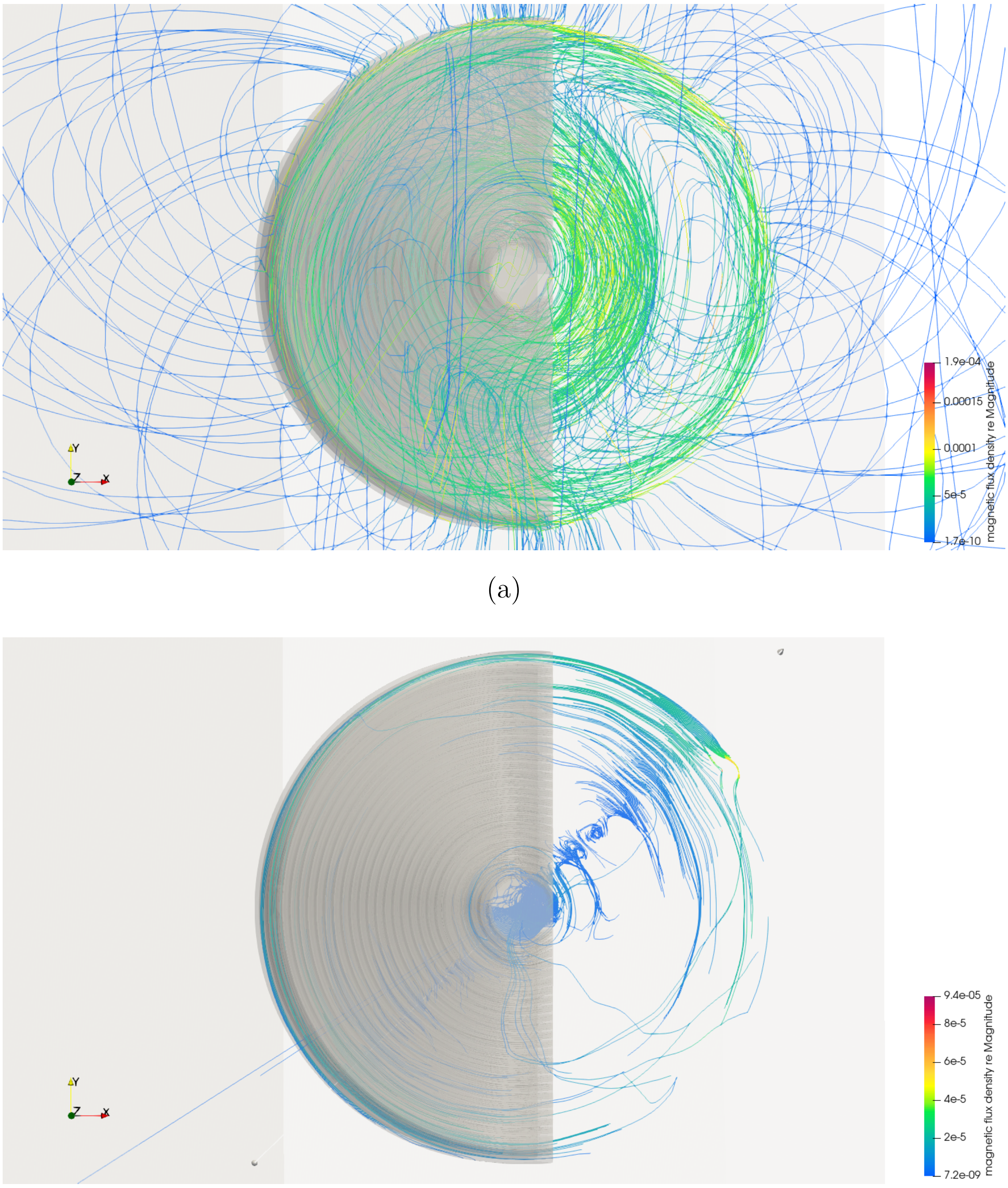

(a)

(b)

Figure 5.12: 3-D visualization of magnetic flux density streamlines within the cell at different frequencies: (a) 5 kHz and (b) 1 MHz.

Electric and magnetic field contours

At 5 kHz, the electric and magnetic field contours are visualized in Figure 5.13. The electric fields are noticed to be maximum in certain region in the top and bottom of the electrode jelly roll. Whereas the magnetic fields are high in the regions near the current collectors and terminals. This helps identify the areas within the battery cell which exhibit high electric and magnetic field strengths, allowing opportunities for design optimization of the cell.

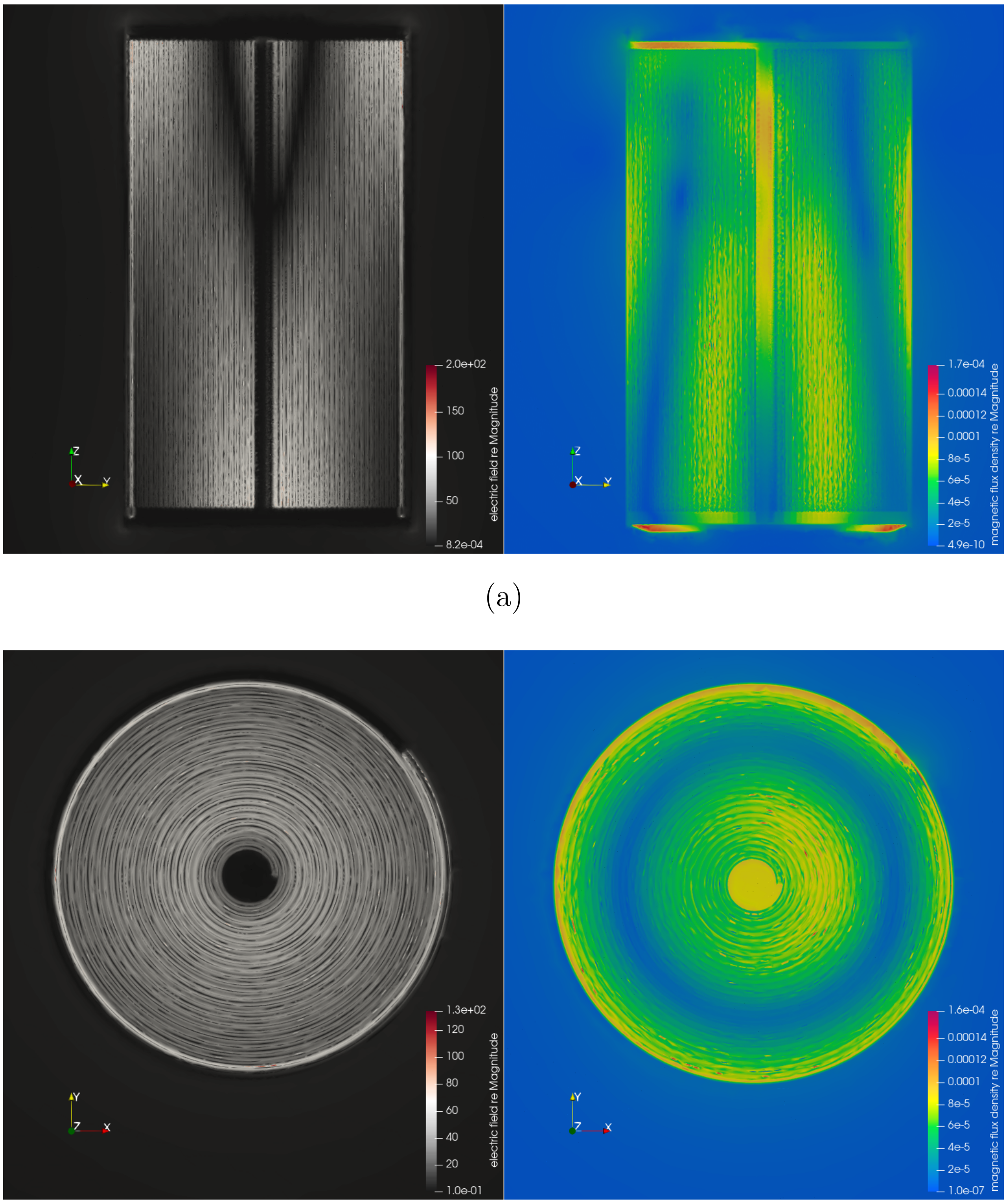

(a)

(b)

Figure 5.13: Electric field and magnetic flux density contours at 5 kHz (a) Side plane and (b) Top-mid plane

5.3.2.2 Thermal parameters

The 3-D representation of temperature distribution within the cell in Figure 5.14 reveals a maximum temperature of 312 K at 5 kHz, located on the cathode terminal and the cathode current collector. The localized heating is attributed to the higher current densities due to skin effect observed on these surfaces, as shown in Figure 5.11. The temperature result account for joule heating, which arises from the heat generated due to flow of current through the cell components.

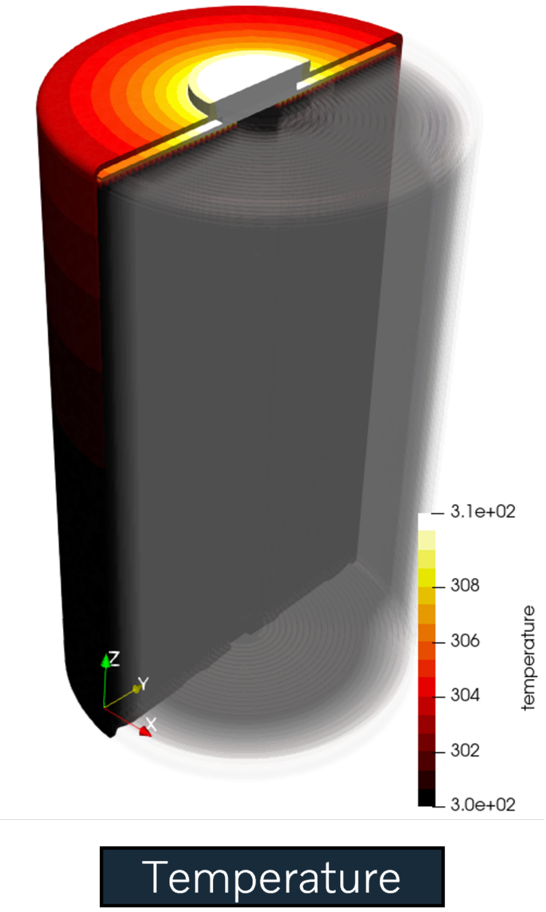

Figure 5.14: 3-D visualization of temperature distribution at 5 kHz

The temperature gradients on the cathode top plate and current collector reflect the maximum temperature regions and the temperature distribution. These results provide insights on the thermal hotspots within the battery cell and can support the decision-making regarding the placement of cooling plates in the battery. This will also enable the investigation of temperature profiles for various cooling arrangements.

5.3.2.3 Structural parameters

Figure 5.15 illustrates the displacement and von Mises stress distribution in the cylindrical cell at a frequency of 5 kHz. A maximum displacement of 160 μm is observed at the cell casing.

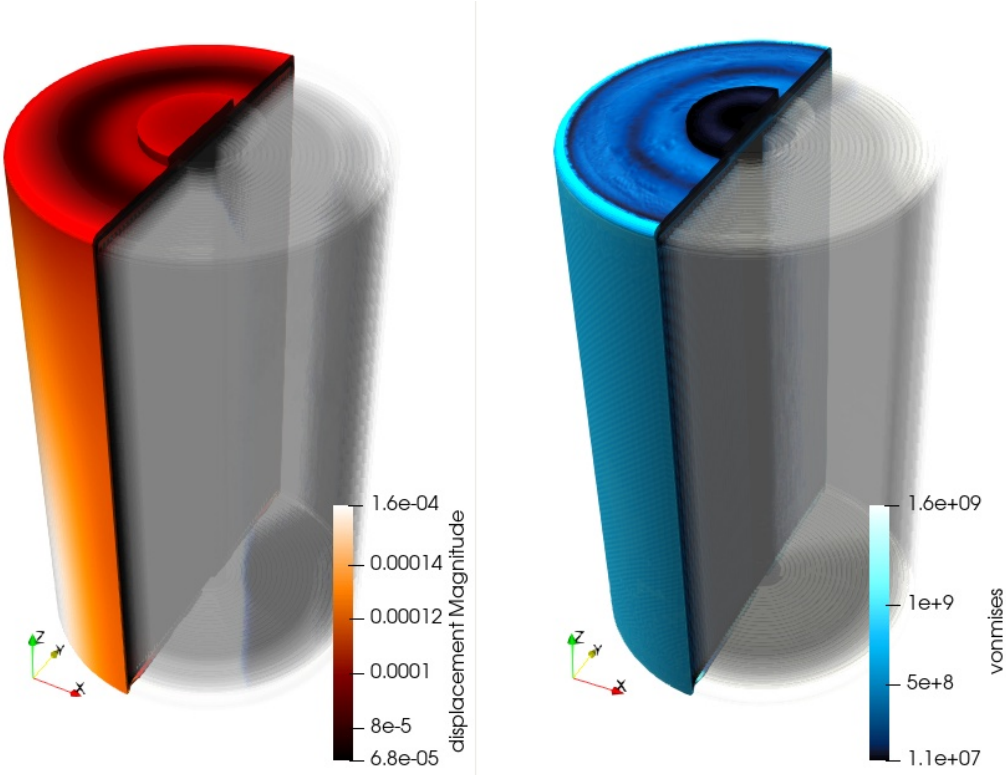

Figure 5.15: 3-D visualization of structural behavior at 5 kHz

The von Mises stresses are found to be higher in regions with large displacements, indicating a correlation between mechanical displacement and internal stress. The highest von Mises stress, observed to be 1.6 GPa, occurs in the cell casing. This force arises from nodal forces in the magnetic simulation and is not a consequence of mechanical forces arising from electrochemical interactions. These von Mises stress results serve as an indicator of potential swelling within the cell. Furthermore, the directional stress components can provide insight into the directionality of the swelling behavior. Analyzing this result for a pack level simulation can support the battery pack design and placement of compression pads in the battery pack.

5.3.3 Simulation model validation

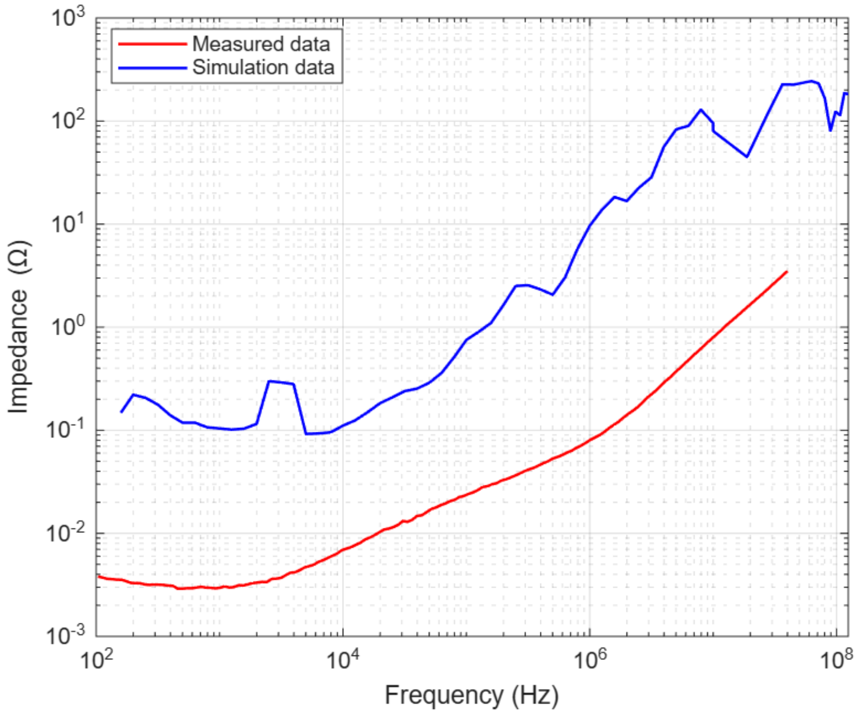

Figure 5.16: Simulation and Experiment comparison; Impedance magnitude Vs frequency for the cylindrical cell

The simulation and experimental data are compared in Figure 5.16. The slopes of the graph between the frequencies 1kHz and 100kHz for both measurement and simulation is found to be 2×10^{-7} and 6×10^{-6} respectively. The difference in slope between the two graphs is 5.8×10^{-6}, which is considered negligible, indicating a consistent trend between the simulation and the measurement results.

Though the overall trend in impedance is similar, the magnitude of impedance is offset. This could be due to the following reasons:

- The CAD model used for the OEM 46XX cell does not fully represent the actual cell design. Especially the current collector and the tabs from the current collector to the electrode terminals does not match the X-ray images in Figure 4.13.
- A few material properties used for the cell components are not validated and might be inaccurate. Particularly the relative permeability and permittivity and their frequency dependence for some of the materials are not found from validated sources. It is important to note that these material parameters contribute significantly to the impedance behavior and magnitude of the cell.
- Material anisotropy is neglected in the simulation due to insufficient data.

Although notable differences exist between the simulation and experimental results, similarities are observed in the impedance behavior. Both cases present a comparable impedance drop in the mid-frequency region and inductive behavior in the high frequency region. The cutoff frequency from the experiment is around the 3kHz region, whereas the simulation has a cutoff frequency around the 8kHz region. This offset indicates a delayed transition to inductive behavior in the simulation model. The cutoff frequency region and overall trend in both cases are also comparable with the bode plots reported in the literature, as illustrated in Figure 3.7.

5.3.4 Simulation model for EMC analysis

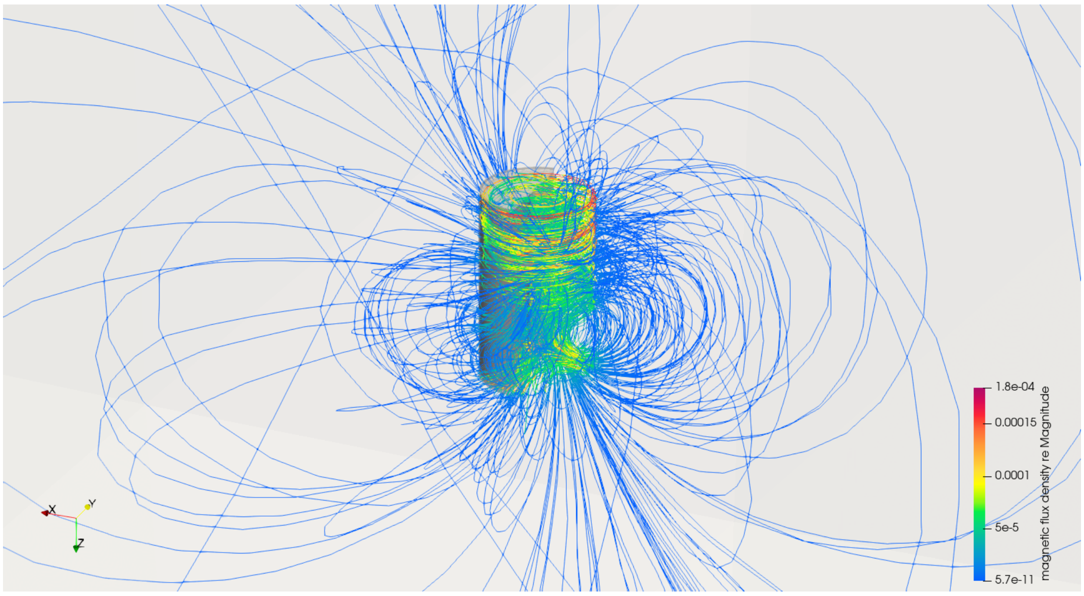

Figure 5.17: 3-D visualization of magnetic flux density streamlines in the far-field surrounding the cell at 5 kHz

Using the developed simulation model, the magnetic flux streamlines surrounding the cell can be visualized, as shown in Figure 5.17. The results clearly demonstrate the formation of closed magnetic loops around the cylindrical cell. The shape and strength of these magnetic fields determine the extent of EMI. From the literature, we know that the EMI emission is proportional to the loop area and the rate of current change [50]. Though it is evident from Figure 5.17 that the area of the magnetic loop is larger, the magnitude of magnetic flux density at 5 kHz is on the order of 5×10^{-11} T, which is far too weak to affect a neighboring cell in the pack. While, a relatively higher magnetic flux density is expected at lower frequencies, such as 1 kHz.

This analysis becomes more significant when the simulation is carried out on a battery pack (including busbars and return loops) instead of a single cell. This simulation extended to a pack level study could potentially help with the following:

- Study magnetic flux interactions and apply suitable EMI suppression methods
- Support the battery pack design (for example, minimize the magnetic flux leakage by reducing the loop area or avoid usage of excessive EMI shielding thereby reduce material, weight, and cost).

- Prevent inductive coupling to nearby sensitive circuits and other electronics.
- Study the parasitic inductance at HF and reduce its contribution to impedance.

5.3.5 Dependency study

5.3.5.1 Mesh element type

To determine the most appropriate mesh element type, both the unstructured (tetra) and hybrid mesh (hexapoly) configurations, as described in Section 3.9, were evaluated. Due to the complexity of the cylindrical cell model, a fully structured mesh is not considered. Figure 5.18 presents the impedance plot obtained using the tetra and hexapoly mesh types. Note that the moving average data filter is applied to both the graphs. The results indicate that the tetra mesh has lower fluctuations in the low frequency region and closely aligns with the hexapoly results. However, at higher frequencies, the tetrahedral mesh displays anomalous deviations from the overall trend. Therefore, hexapoly mesh element was selected for this study.

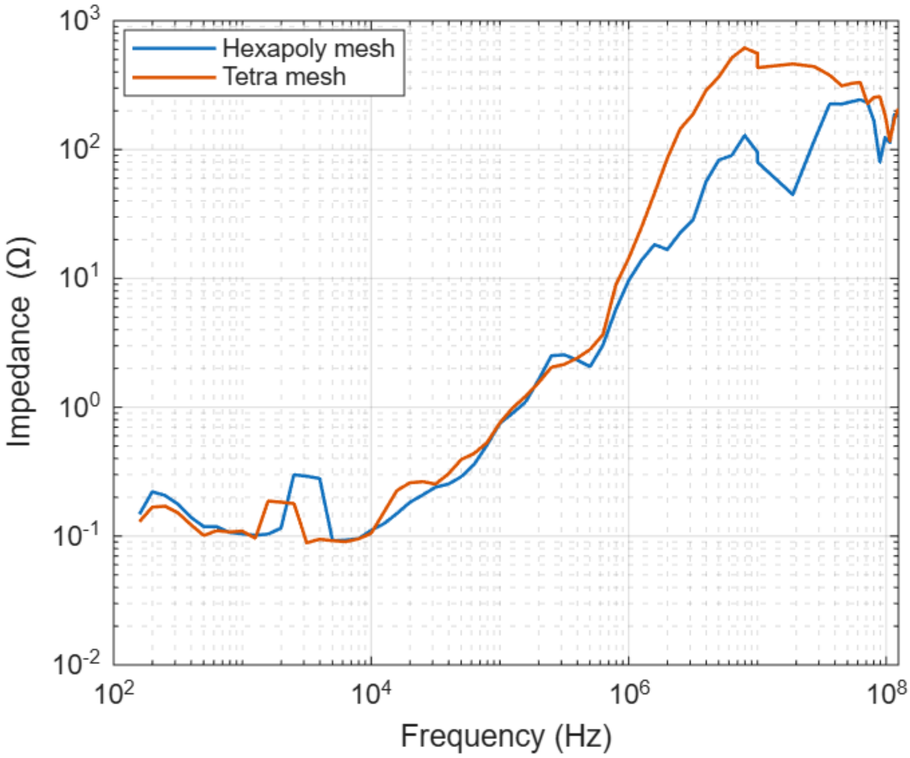

Figure 5.18: Mesh comparision between hexapoly and tetrahedral mesh elements for cylindrical cell model

5.3.5.2 Number of simulation cores

The simulation time in the cluster is affected by the number of core partitions. Initially, five different partitions were evaluated in the frequency range of 100 Hz to 800 Hz to estimate CPU time, as shown in Figure 5.19 (a). The partitions with the lowest computation times were studied in further detail. Figure 5.19 (b) illustrates the computation time taken from 100 Hz to 4 MHz for the chosen partitions.

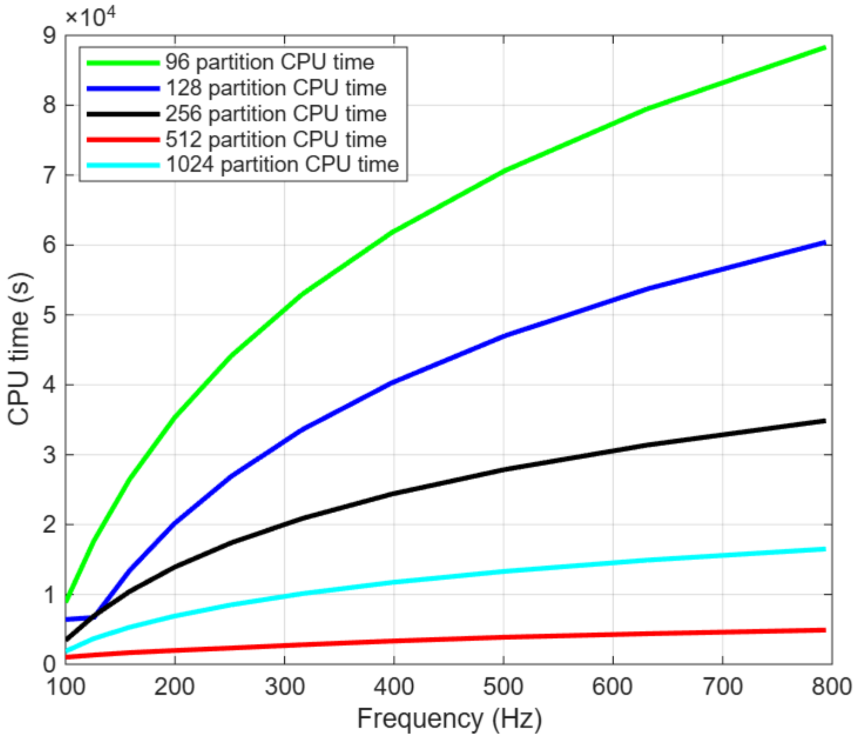

(a)

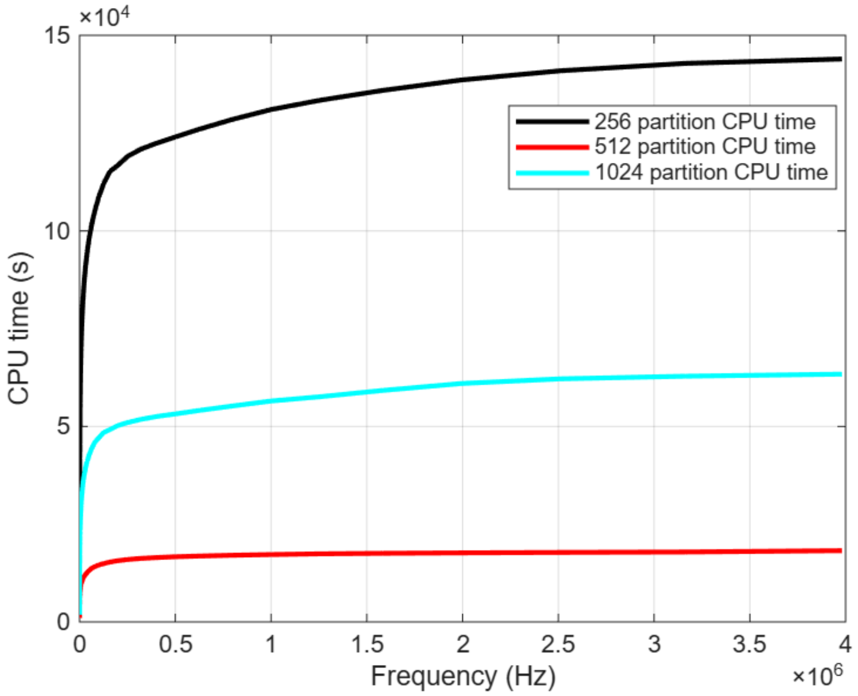

(b)

Figure 5.19: (a) CPU time Vs Frequency for different simulation core partitions from 100 to 800 Hz and (b) CPU time Vs Frequency for the filtered simulation core partitions from 100 Hz to 4 MHz

Computational time taken to reach 4 MHz frequency:

- 256 partitions – 40 hours
- 512 partitions – 24.5 hours
- 1024 partitions – 17.5 hours

Difference in CPU time to reach 4 MHz frequency:

- Between 512 and 1024 partitions: 7 hours difference
- Between 256 and 512 partitions: 15.5 hours difference

In order to minimize computation time and manage cluster load effectively, the simulations in this study were conducted using a 512-core partition.

5.3.6 AI governed design of current collector

The CAD geometry of the different candidates in Figure 5.20 show the current collector design modified using GA. The current collector was chosen for optimization, as it exhibits the highest current density within the cell, acting as the bottleneck for current accumulation, as shown in the current density distribution in Figure 5.11.

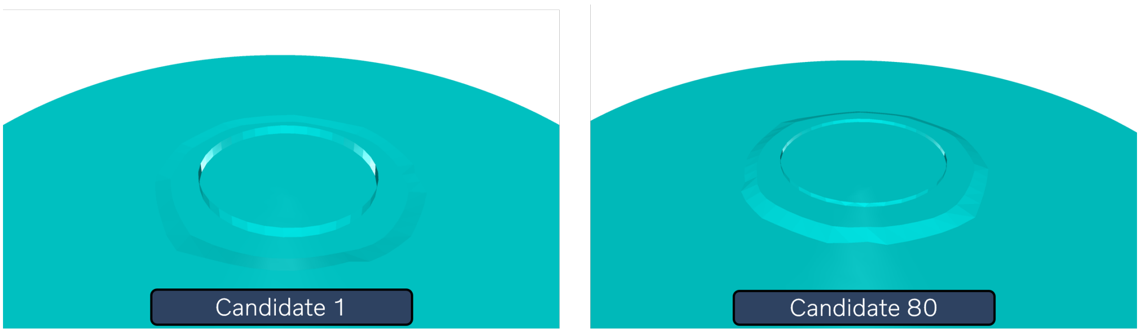

Figure 5.20: Geometry of different candidates generated using GA

Figure 5.21 illustrates all the candidate solutions generated during AI search for the best design of the current collector for the specified multiphysics objectives. As depicted, this is achieved by using line plots, histograms and Pareto front. The change in objective variables and geometry are monitored during the AI run simulation using the line plots in blue. Representative histograms of objective variables are shown in red, while cross-variations between objective variables are illustrated in green, highlighting Pareto-optimal solutions. Following the extensive data generation and exploration for optimal solution using GA, a candidate solution was identified that achieves maximized current (reduced impedance), reduced weight, and reduced displacement for the cathode current collector.

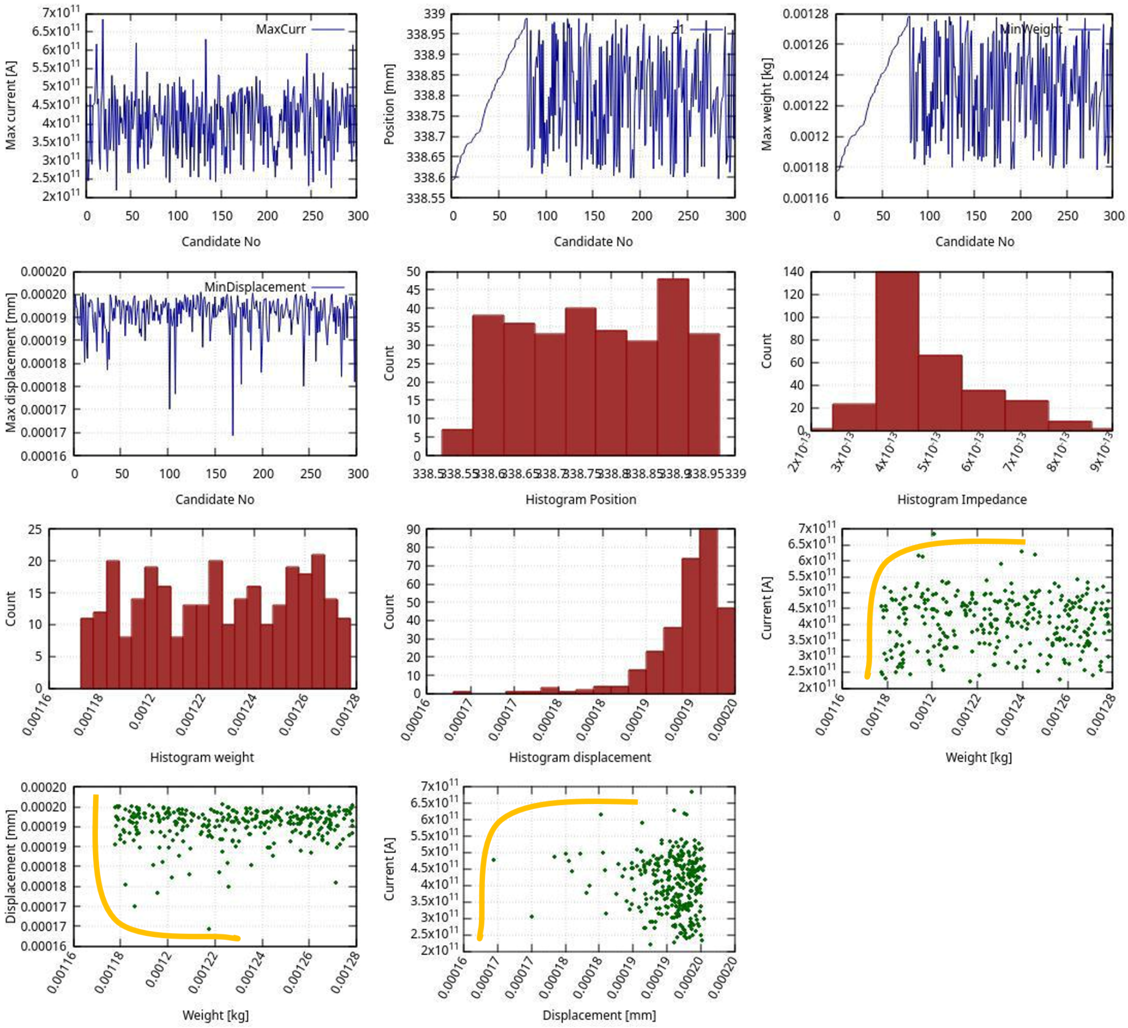

Figure 5.21: AI based design selection for current collector using GA

Chapter 6

Conclusion

6.1 Overview

The high-fidelity model of a li-ion Battery cell presented in this thesis is simulated across multiple disciplines, using a robust simulation setup and the cell behavior at high frequencies, HF impedance estimation, Analysis for EMI/EMC & the impact of modifications in the cell layers have been researched in detail.

The initial chapters discuss impedance in general, components of impedance, their dependence on frequency and impedance of a battery cell. The impedance estimation methods and measurement methods for electrical systems are also discussed. The governing laws of electromagnetism, thermal behavior including conduction, convection, Joule heating & linear elasticity have been discussed in context of this research work. Meshing for FEM, types of meshes are discussed in these chapters as this thesis deals with 3D modeling and simulation.

The project workflow, software information and solver descriptions have been discussed in these chapters. The implemented case setup for the harmonic wire including mesh configuration, boundary and initial condition definition and solver setup is discussed in the methodology chapter. This chapter also explains the case setup for the coin cell and the cylindrical OEM cell including the 3D model, meshing, boundary and initial conditions and experimental setup and tests have also been discussed in detail.

The post processed plots and images of the wire including the polyline data and the comparison between simulation and experiment have been done in the Analysis Section. Results from the coin cell simulation including the polyline data for model validation, impedance plots and visualization of field variables are also presented in this chapter. The processed results for the cylindrical cell, including the impedance curve across the swept frequency range is presented along with visualization of various field variables like the potential, current density, magnetic flux density and temperature of cell to study joule heating. The structural displacement due to the nodal forces are also analyzed. The experimental results are also published here and the comparison between the simulation and experiment was performed.

6.2 Observations from results

The following observations can be drawn based on the obtained results:

- The cylindrical cell transitions the behavior from dominant capacitive to inductive behavior at around 8 kHz in the simulation and around 5 kHz in the experimental results. This is verified by the literature, where the cutoff frequency is observed to be approximately 1–5 kHz, depending on the cell type.
- Impedance results comparing simulation and experimental data for the harmonic wire model, show a deviation of 11% at 5 kHz, indicating a reasonable correlation in the high frequency region. Thereby confirming the applicability of the solver setup.
- The visualization of the cylindrical cell at 5 kHz reveals the highest current density and the maximum temperature in the current collector region. This is caused by the accumulation of current from the terminals and electrodes in the current collector. Whereas the highest displacement and von Mises stress is observed in the cell casing indicating swelling behavior of the cell.
- Cylindrical cell visualization at 5 kHz further reveals the peak value of the electric fields at the top and bottom regions of the electrode jelly roll. The magnetic fields are strongest near the current collectors and terminals.
- For the cylindrical 46XX cell, the impedance comparison between the simulation and experiment indicate similar overall trend in behavior, as shown by the comparable slopes, despite the offset in magnitude.
- The visualization of the magnetic field lines at 5 kHz in the cell's far-field reveals a large magnetic loop area, with field magnitudes in the order of 10^{-11}. This field strength is expected to be too weak to induce significant EMI, whereas lower frequency fields are expected to have a greater influence on EMI. This result also provides valuable insight for the implementation of effective EMI suppression techniques, especially when scaling the model to a battery pack study.
- The developed MOGA-based computational framework has been used to identify an optimized current collector design that minimizes impedance (maximizing current), weight, and displacement.

6.3 Future work

This section provides insights on some of the possible future work using the 3D FEM simulation script and genetic algorithm developed during this thesis.

6.3.1 Possible improvements using ElmerFEM

6.3.1.1 Accurate CAD model

Perform the simulation using a cylindrical cell CAD model that accurately matches the physical cell to correlate the cylindrical cell results. From the obtained results, the measurement and simulation have a reasonable correlation for the wire model. This validates the electromagnetic solver outputs and the solver configurations used in this thesis. Therefore, an accurate CAD model of the cylindrical cell is expected have reasonable correlation between simulation and measurement.

6.3.1.2 Alternate solvers

In ElmerFEM, other solver options are available for electromagnetic computations, such as VectorHelmholtz Solver. The implementation of the VectorHelmholtz solver presents notable challenges, particularly in determining the boundary conditions and body force inputs. For this solver, the boundary condition requires a complex-valued electric field vector defined on the edge elements, whereas the body force input is given in terms of the current density. If the required inputs are available, a comparison of the results for the cylindrical cell between the VectorHelmholtz and MagnetoDynamics solvers can be performed for additional validation.

6.3.1.3 Custom solvers

The computation tool allows to compile a purpose-tailored solver (written in Fortran) and integrate it into the existing Elmer solver framework. Chapter 19 of the ElmerSolver manual [40] describes the foundational programming interface and the usage of built-in data structures, routines, and utilities for custom extensions. It also supports the user-defined functions to define properties or point-wise (individual nodes or elements) expressions for material parameters (e.g., temperature-dependent conductivity), boundary conditions, or body forces. This could enable greater flexibility in the simulation by allowing case-specific requirements.

6.3.1.4 Validated material properties

Measurements can be conducted on the materials used in the cylindrical cell to validate the properties such as electrical conductivity, permittivity, and other material parameters that impact the impedance behavior. These measurements may be conducted using instruments such as impedance analyzers, VNA, and spectrographic analyzers. Furthermore, these instruments enable the measurement of material properties as a function of frequency and the anisotropy. This allows the model setup to represent the realistic material behaviors.

6.3.1.5 In-depth study of thermal performance

In the cylindrical cell model, the HTC applied as the boundary condition corresponds to natural convection, whereas in reality the battery cells are subjected to liquid cooling. This allows scope for studying the thermal behavior by using a realistic HTC value for liquid cooling or based on experimental measurements. The visualization also enables the investigation of temperature profiles by modifying the HTC for various cooling plate configurations, such as top cooling, side cooling and bottom cooling arrangements. The cooling configuration influences the cell temperature, and the resulting impact on impedance can also be systematically studied.

6.3.2 Scale simulation to battery module/pack

This model can further be scaled to a module level or a pack level study to investigate different parameters like parasitic capacitance, cross-coupling effects of cells and impact of components like busbars and spot welds on the cell. This helps in studying the EMI effects of the module or the pack on the electronics in it's vicinity and designing suitable EMC filters.

Scaling the simulation model to a battery module or a pack has increased complications due to the complexity of the CAD geometry. For eg, a module consists of the cell holders, cell contact systems (busbars), depending on the battery system architecture a Cell Monitoring Unit (CMU) and structural components apart from the battery cell. This introduces complexity in terms of size of the geometry file, performing mesh refinement, acquiring material data, assigning boundary conditions and computational load on the cluster.

6.3.3 Future applications of genetic algorithm

The developed multi-objective genetic algorithm can also be used for designing the optimal anode current collector especially for the charging cycle. This is essential due to the significant accumulation of current in the anode current collector during the charging cycle. Applying MOGA allows for the balancing of multidisciplinary design objectives and avoid bottlenecks in both the current collectors with respect to the current distribution, weight and mechanical displacement.

Genetic algorithm framework can be further scaled to be applied on the battery module/pack with objective functions to minimize magnetic field strength in the far-field, minimize vonmises stress and weight of the cell casing and module/pack structures. This optimization may help design the battery cell casing and structural components of the module and pack for EMC purpose.

The control parameters for MOGA can be further modified. Increasing the population size may enhance diversity and improve coverage of the solution space. The Pareto fronts for displacement vs. weight and current vs. displacement indicate that the solutions are stagnating, with clustering observed around specific regions of the solution space. MOGA simulation performed in this thesis has a population size of 80 as discussed in Table 4.12. This can be increased to generate more individuals thereby improve diversity and add more genetic material to improve the effectiveness of crossover and mutation. Larger populations may stress the computational resources hence balancing the population size and computational load is important.

Increasing the maximum number of function evaluations beyond 300 could improve convergence by allowing more generations during the simulation. Increased number of generations allows the population to evolve and refine the solutions.

The MOGA-generated dataset can be used to train a neural network model, enabling rapid prediction of optimal designs. Like large language models (LLMs), it learns complex patterns, reducing computational cost and accelerating future optimization.

Bibliography

[1] Volvo Cars. Volvo Cars adjusts electrification ambitions, remains committed to fully electric future. Global Newsroom; 4 Sep 2024. Available from: `https://www.media.volvocars.com/global/en-gb/media/pressreleases/333213/`

[2] United Nations. Sustainable Development Goals. `https://sdgs.un.org/goals`

[3] Parschau, A., Degler, D., Allmendinger, F., Birke, K. P., & Fill, A. (2023). Investigation of high-frequency pulse charging profiles with different frequencies, duty cycles and end-of-charge voltages. *Journal of Energy Storage*, 74, 109500. `https://doi.org/10.1016/j.est.2023.109500`

[4] Hambley, A. R. (2013). *Electrical Engineering: Principles and Applications* (6th ed.). Pearson.

[5] Yang, Q., Xu, J., Cao, B., & Li, X. (2017). A simplified fractional order impedance model for lithium-ion batteries. *PLoS ONE*, 12(2), e0172424. `https://doi.org/10.1371/journal.pone.0172424`

[6] Tavares, A. H. B. M., Esche, F. v. d., Luiz, S. O. D., et al. (2024). A model for a lithium-polymer battery. *Journal of Control, Automation and Electrical Systems*, 35, 625–638. `https://doi.org/10.1007/s40313-024-01081-1`

[7] Pan, Z., Li, W., & Xia, Y. (2020). Experiments and 3D detailed modeling for a pouch battery cell under impact loading. *Journal of Energy Storage*, 27, 101016. `https://doi.org/10.1016/j.est.2019.101016`

[8] Z. Wang, J. Ma and L. Zhang, Finite Element Thermal Model and Simulation for a Cylindrical Li-Ion Battery, in IEEE Access, vol. 5, pp. 15372-15379, 2017. `https://doi.org/10.1109/ACCESS.2017.2723436`

[9] Landinger, T.F., Schwarzberger, G., & Jossen, A. (2020). A physical-based high-frequency model. *IEEE Trans. Electromagnetic Compatibility*, 62(4), 1524-1533. `https://doi.org/10.1109/TEMC.2020.2979877`

[10] Landinger, T.F., Schwarzberger, G., & Jossen, A. (2021). High frequency impedance characteristics of cylindrical lithium-ion cells. *Journal of Power Sources*, 488, 229463. `https://doi.org/10.1016/j.jpowsour.2021.229463`

[11] Keller, R.B. (2023). Skin Effect. In: *Design for Electromagnetic Compatibility - In a Nutshell.* Springer. `https://doi.org/10.1007/978-3-031-14186-7_10`

[12] Zhang, J., & Lv, Y. (2019). High Frequency Impedance and EMI Suppression of Lithium-Ion Pack. *SAE Technical Paper.*

[13] Henriksson, A., Lektenius, J., Bergqvist, A., et al. (2018). *RIFEL – Ripple and Electromagnetic Fields in Electric Vehicles: Technical Report.*

[14] Ramallo-Gonzalez, A. P., Eames, M., & Coley, D. (2013). Lumped parameter models for building thermal modelling. *Energy and Buildings*, 60, 174–184. `https://doi.org/10.1016/j.enbuild.2013.01.014`

[15] Keysight Technologies. (2013). *Impedance Measurement Handbook* (6th ed.). `https://www.keysight.com/us/en/assets/7018-06840/application-notes/5950-3000.pdf`

[16] OMICRON Lab. B-WIC & B-SMC Impedance Test Fixtures User Manual. OMICRON electronics, 2020.

[17] Toshiba Electronic Devices and Storage Corporation. What is Kelvin connection? [Internet]. Tokyo (JP): Toshiba Electronic Devices and Storage Corporation; [cited 2025 Sep 22]. Available from: https://toshiba.semicon-storage.com/ap-en/semiconductor/knowledge/faq/mosfet/what-is-kelvin-connection.html

[18] Biologic. Why use EIS for battery research? [Internet]. Seyssinet-Pariset (FR): Biologic; [cited 2025 Sep 22]. Available from: https://www.biologic.net/topics/why-use-electrochemical-impedance-spectroscopy-for-battery-research/

[19] Henriksson, A. (2025). *Impedance Measurement Techniques for DC-Biased Systems.* MSc Thesis, Chalmers University of Technology. `http://hdl.handle.net/20.500.12380/309307`

[20] Ariyoshi, K., Mineshige, A., Takeno, M., Fukutsuka, T., Abe, T., Uchida, S., & Siroma, Z. (2022). Electrochemical impedance spectroscopy part 2: applications. *Electrochemistry*, 90(10), 102008. `https://doi.org/10.5796/electrochemistry.22-66080`

[21] Haslach Jr, H. W. (2010). Electromagnetism and Joule heating. In *Maximum Dissipation Thermodynamics.* Springer. `https://doi.org/10.1007/978-1-4419-7765-6_10`

[22] Bergman, T. L., Lavine, A. S., Incropera, F. P., & DeWitt, D. P. (2011). *Fundamentals of Heat and Mass Transfer* (7th ed.). John Wiley & Sons.

[23] Timoshenko, S., & Goodier, J. N. (1970). *Theory of Elasticity* (3rd ed.). McGraw-Hill.

[24] Elmer FEM. `https://www.elmerfem.org/blog/`

[25] Ruokolainen, J., Malinen, M., Råback, P., Zwinger, T., Pursula, A., & Byckling, M. (2021). *ElmerModels Manual.* CSC – IT Center for Science.

[26] Ruggiero, A., D'Amato, R., & Affatato, S. (2019). Comparison of meshing strategies in THR finite element modelling. *Materials*, 12(14), 2332. `https://doi.org/10.3390/ma12142332`

[27] Sadrehaghighi, I. (2022). *Unstructured Meshing for CFD.* CFD Open series, Patch 2.60.

[28] BETA CAE Systems. ANSA Pre-Processor. `http://www.beta-cae.com/ansa.htm`

[29] Jafari Kaleybar H, Davoodi M, Brenna M, Zaninelli D. Applications of Genetic Algorithm and Its Variants in Rail Vehicle Systems: A Bibliometric Analysis and Comprehensive Review. IEEE Access. 2023; 11:68972-68993. `https://doi.org/10.1109/ACCESS.2023.3292790`

[30] Bhoskar T, Kulkarni OK, Kulkarni NK, Patekar SL, Kakandikar GM, Nandedkar VM. Genetic Algorithm and Its Applications to Mechanical Engineering: A Review. Mater Today Proc. 2015;2(4-5):2624-2630. `https://doi.org/10.1016/j.matpr.2015.07.214`

[31] Adams BM, Bohnhoff WJ, Dalbey KR, Ebeida MS, Eddy JP, Eldred MS, et al. Dakota, A Multilevel Parallel Object-Oriented Framework for Design Optimization, Parameter Estimation, Uncertainty Quantification, and Sensitivity Analysis: Version 6.16 User's Manual. Sandia National Laboratories. Report No. SAND2022-6171; May 2022.

[32] Sandia National Laboratories. moga — Multi-objective Genetic Algorithm (Dakota Documentation 6.20.0). Albuquerque (NM): Sandia National Laboratories, 2023. Available from: `https://snl-dakota.github.io/docs/6.20.0/users/usingdakota/reference/method-moga.html`

[33] Gmsh. `https://gmsh.info/`

[34] OMICRON Lab. Bode 100 Vector Network Analyzer. `https://www.omicron-lab.com/products/vector-network-analysis/bode-100/`

[35] Spyder IDE. `https://www.spyder-ide.org/`

[36] MathWorks, Inc. MATLAB. `https://se.mathworks.com/products/matlab.html`

[37] ParaView. `https://www.paraview.org/`

[38] Sandia National Laboratories. Dakota [Internet]. Albuquerque (NM): Sandia National Laboratories; updated 2025 May 15. Available from: `https://dakota.sandia.gov/`

[39] Williams T, Kelley C, et al. Gnuplot [Internet]. Available from: `http://www.gnuplot.info/`

[40] Ruokolainen, J., Malinen, M., Råback, P., Zwinger, T., Pursula, A., & Byckling, M. (2021). *ElmerSolver Manual.* CSC – IT Center for Science. `http://www.csc.fi/elmer`

[41] CSC – IT Center for Science. *Elmer Tutorials.* `https://www.nic.funet.fi/pub/sci/physics/elmer/doc/ElmerTutorials.pdf`

[42] GrabCAD. CR3032 lithium-sulphur coin battery cell-1. `https://grabcad.com/library/cr3032-lithium-sulphur-coin-battery-cell-1`

[43] COMSOL, Inc. Material Library. `https://www.comsol.com/material-library`

[44] Cardarelli, F. (2008). *Materials Handbook.* Springer.

[45] Balanis, C. A. (2016). *Antenna Theory: Analysis and Design.* John Wiley & Sons.

[46] Stutzman, W. L., & Thiele, G. A. (2012). *Antenna Theory and Design.* John Wiley & Sons.

[47] Ank, M., et al. (2023). Lithium-Ion Cells in Automotive Applications: Tesla 4680 Cylindrical Cell Teardown and Characterization. *Journal of The Electrochemical Society*, 170(12), 120536.

[48] Engineering ToolBox. Material Properties. `https://www.engineeringtoolbox.com/material-properties-t_24.html`

[49] Fluke Corporation. Fluke Digital Multimeters. `https://www.fluke.com/en-us/products/electrical-testing/digital-multimeters`

[50] Accurate models for evaluating the direct conducted and radiated emissions from integrated circuits. *Applied Sciences*, 8(4), 477. (2018). `https://doi.org/10.3390/app8040477`

DEPARTMENT OF ELECTRICAL ENGINEERING,
CHALMERS UNIVERSITY OF TECHNOLOGY
Gothenburg, Sweden
www.chalmers.se

CHALMERS
UNIVERSITY OF TECHNOLOGY